HHS Public Access

Author manuscript

Nature. Author manuscript; available in PMC 2020 December 22.

Published in final edited form as:

Nature. 2019 December ; 576(7785): 121–125. doi:10.1038/s41586-019-1772-4.

Sensorimotor experience remaps visual input to a heading direction network

Yvette E. Fisher, **Jenny Lu**, **Isabel D'Alessandro**, **Rachel I. Wilson**

Harvard Medical School, 220 Longwood Ave., Boston, MA 02115, USA

Abstract

In the *Drosophila* brain, "compass neurons" track the orientation of the body and head during navigation (the fly's heading)[1,2]. In the absence of visual cues, the compass neuron network estimates heading by integrating self-movement signals over time[3,4]. When a visual cue is present, the network's estimate is more accurate[1,3]. Visual inputs to compass neurons are thought to originate from inhibitory neurons called R neurons; R neuron receptive fields tile visual space[5]. The axon of each R neuron overlaps with the dendrites of every compass neuron[6], raising the question of how visual cues are integrated into the compass. Here, using *in vivo* whole-cell recordings, we show that a visual cue can evoke synaptic inhibition in compass neurons, and R neurons mediate this inhibition. Each compass neuron is only inhibited by specific visual cue positions, implying that many potential connections from R neurons onto compass neurons are actually weak or silent. Notably, we show that the pattern of visually evoked inhibition can reorganize over minutes as the fly explores an altered virtual reality environment. Using ensemble calcium imaging, we demonstrate that this reorganization causes persistent changes in the compass coordinate frame. Our results suggest a model where correlated pre- and postsynaptic activity triggers associative long-term synaptic depression of visually evoked inhibition in compass neurons. Our findings provide evidence for the theoretical proposal that associative plasticity of sensory inputs, when combined with attractor dynamics, can reconcile self-movement information with changing external cues to generate a coherent sense of direction[7–12].

The compass neurons in the *Drosophila* brain exhibit some resemblance to the head direction cells of the mammalian brain[13–16]. Visual cues stabilize the tuning preferences of mammalian head direction cells[15], and when the experimenter rotates a visual cue to a new horizontal position, the preferences of all the head direction neurons rotate together[14,16]. It has been proposed that the mammalian head direction system represents a ring attractor – a network whose global dynamics exhibit multiple stable states which unfold in a repeated

---

Correspondence and requests for materials should be addressed to R.I.W. (rachel_wilson@hms.harvard.edu).

Author Contributions

Y.E.F, J.L., and R.I.W. designed the study. Y.E.F. performed and analyzed electrophysiology experiments. J.L. performed and analyzed 2-photon calcium imaging experiments. I.D. performed and analyzed confocal imaging experiments. Y.E.F and R.I.W. wrote the manuscript with input from J.L. and I.D.

The authors declare no competing financial interests.

Data availability statement: The datasets generated during and/or analyzed during the current study are available from the corresponding author on reasonable request.

Code availability statement: Analysis code is available at https://github.com/wilsonlab/FisherLuDAlessandroWilson_AnalysisCode

sequence in response to an input[7,17,18]. However, we do not know how visual cues anchor the mammalian head-direction system at a mechanistic level. It has been suggested that Hebbian synaptic plasticity of visual inputs could enforce the correct mapping between sensory cue and attractor network states[7].

Similar to mammalian head-direction cells, *Drosophila* compass neurons (called E-PG neurons) exhibit properties of a ring attractor[2]. Indeed, the dendrites of E-PG neurons are arranged in a ring in the brain (Fig. 1a). At any point in time, there is one "bump" of activity in the E-PG ensemble which rotates as the fly turns[1]. This network receives continuous input from brain regions that track the fly's rotational velocity via optic flow signals, proprioceptive signals, and/or motor efference signals[3,4]. These rotational velocity inputs push the bump around the circle. Visual cues make the bump's position more accurate and stable[1,3]. However, we do not know whether visual inputs to E-PG neurons are plastic: The "offset" between the E-PG bump and the visual world is different in different individuals and it can occasionally change unpredictably within an individual[1,3], but network instability alone is not evidence for synaptic plasticity.

Although the axon of each R neuron overlaps with every E-PG dendrite (Fig. 1b), R→E-PG connections should be functionally selective; otherwise, information about the position of a visual cue would be discarded. We hypothesized that the all-to-all matrix of R→E-PG anatomical connections (Fig. 1c) represents a set of "potential" functional connections which can be re-patterned during spatial learning. We therefore set out to test two hypotheses – first, that individual E-PG neurons respond selectively to specific visual cue positions, and second, that changes in visual-heading associations can trigger systematic, time-locked changes in the pattern of E-PG visual inputs.

Results

Our first challenge was to isolate the synaptic input to E-PG neurons that is related to visual cue position, separate from the synaptic input related to the fly's rotational velocity. We reasoned that this should be possible if we flashed visual cues transiently at randomized positions, preventing the fly from behaviorally fixating the stimulus. We therefore performed *in vivo* whole-cell recordings from E-PG neurons while flashing a bright vertical bar on a dark circular panorama at randomized horizontal positions (Fig. 1d). In a typical neuron, we observed hyperpolarization that was time-locked to flashes at specific positions (Fig. 1e). To verify that these neural responses are not related to the fly's rotational velocity, we analyzed the movement of the air-cushioned ball that the fly was standing on (Extended Data Fig. 1). Neural responses were unrelated to the fly's rotational velocity around the time of the visual flash (Fig. 1e), and there was no correlation between the fly's rotational velocity and the flash (Fig. 1f). Therefore, we can interpret visually-locked responses as synaptic inputs related to visual cue position. We call this the cell's "visual receptive field". The finding of visually-evoked hyperpolarization is consistent with the fact that R neurons release the inhibitory neurotransmitter γ-aminobutyric acid (GABA)[19,20].

In almost every E-PG neuron, we found that some visual cue positions elicited hyperpolarization while other positions elicited no hyperpolarization (Fig. 1e,g). This

implies that each E-PG neuron receives relatively strong input from some R neurons but weak or nonexistent input from other R neurons. In about half of E-PG neurons, we also found that some cue positions elicited depolarization (Fig. 1g). Depolarization may represent disinhibition: because there is ongoing mutual inhibition between E-PG neurons[2], a visual cue that inhibits one E-PG neuron will disinhibit other E-PG neurons.

We found that different E-PG neurons had distinct visual receptive fields (Fig. 1g). When we sorted cells by the position eliciting minimal hyperpolarization; we found a uniform mapping of cue positions onto E-PG neurons. Notably, hyperpolarization was more prominent for lateral cue positions (Fig. 1g, Extended Data Fig. 2); this spatial bias is probably inherited from R neurons, because R neuron receptive fields are similarly biased towards lateral positions[5].

When we managed to record sequentially from two adjacent E-PG neurons in the same brain, we found they had adjacent receptive fields adjacent receptive fields, as we would expect (Extended Data Fig. 3). However, when we pooled data across brains, we found no systematic relationship between the location of the E-PG neuron's dendrites and its receptive field (Fig. 1h). Therefore, the mapping from visual space to compass coordinates is different across individuals.

Next, we asked how a neuron's visual receptive field compares with its heading tuning. To measure heading tuning, we allowed the fly to walk in closed-loop virtual reality (VR) where the horizontal position of the cue was locked to the fly's virtual heading (Fig. 2a,b). We periodically paused VR to map the same neuron's visual receptive field using brief random flashes. In most neurons, we found that the visual receptive field was correlated with heading tuning (Fig. 2c–d, Extended Data Fig. 3 & 4). This result is notable because heading tuning reflects not only synaptic inputs related to visual cue position, but also synaptic inputs related to the fly's rotational velocity. Imperfect alignment between these inputs may explain why some neurons showed poor correlations (Fig. 2d).

To confirm that R neurons are actually the source of visual responses in E-PG cells, we focused on two R neuron types (R2 and R4d) that respond to sparse visual cues[5]. First, we used whole-cell recordings to confirm that these R neuron types can be excited by the visual cue (Fig. 3a). Second, we verified that optogenetically activating either R2 or R4d neurons inhibits E-PG neurons (Fig. 3b). Third, we established that R neurons are required for normal visually evoked hyperpolarization in E-PG neurons. We used two independent driver lines to hyperpolarize R2 or 4d neurons by overexpressing the potassium channel Kir2.1 (Extended Data Fig. 5), and we confirmed that visually evoked hyperpolarization was attenuated (Fig. 3c, Extended Data Fig. 6). In both genotypes, a few E-PG neurons still showed some visual responses, likely because neither driver line achieves complete coverage of R2/4d neurons (Extended data Fig. 5, 6).

Next, we turned to our second hypothesis – that changes in visual-heading associations can trigger systematic, time-locked changes in E-PG visual receptive fields. After allowing the fly to navigate in VR with one visual cue (the pre-training block), we switched to VR with two cues positioned 180° degrees apart (the training block). In the training block, a full turn

and a half-turn will arrive at an identical view of the world, meaning the correlation between rotational velocity signals and visual cue position signals will be altered.

To assess the effect of training on network dynamics, we imaged calcium signals from the entire E-PG ensemble (Fig. 4a). During pre-training, there was a stable offset between the visual environment and the E-PG bump (Fig. 4b–c). During training, the offset toggled between two values ~180° apart. This result is expected, because there are two equally-valid interpretations of the visual scene, yet only one bump can exist in the E-PG ensemble[2]. When the fly made a 360° turn, we often saw the bump flow twice around 180° of the E-PG ensemble, skipping over the other 180° (Fig. 4a–c). Rotational velocity inputs to the E-PG network should drive the bump to traverse the full circle during a full turn[3,4]; the “skipping over” phenomenon thus implies the dominance of visual position inputs over angular velocity inputs. The E-PG neurons that were traversed twice essentially displayed two preferred heading directions; this is reminiscent of the finding that some rat head direction cells show two preferred directions in an environment with two-fold rotational symmetry[21].

Upon returning to a one-cue environment (post-training), the offset sometimes immediately settled into its original value. Often, however, this was not the case. Rather, the offset continued to toggle for several minutes, or else it immediately settled in a new value rather than the original one (Fig. 4d–e). Both of the latter two outcomes suggest a persistent, systematic change in the way that visual cues are mapped onto E-PG neurons. We observed one of the latter outcomes in half of our experiments (Fig. 4e, Extended Data Fig. 7).

Finally, to investigate whether training changes visual receptive fields, we returned to E-PG whole-cell recordings (Fig. 5a). We began each experiment with one visual cue in VR (pre-training). We then switched to two visual cues in VR (training). Between each block of VR, we periodically paused to map the neuron’s receptive field with brief random flashes. Whereas we used a 360° panorama during calcium imaging, the spatial constraints of electrophysiology required us to map the 360° environment onto a 270° panorama[1,10].

During the training block, we found that some E-PG neurons were strongly modulated by the fly’s heading. In these neurons, training produced striking changes in the visual receptive field. These changes were bidirectional (Fig. 5b), suggesting that visually evoked inhibition was depressed for some cue locations and potentiated for others. We quantified these changes by summing the absolute value of the change in the receptive field across all cue positions (“absolute change”, Fig. 5c). We also measured the change in the shape of the receptive field (Fig. 5c). These metrics were correlated across experiments (Fig. 5d); we never saw a large absolute change in the receptive field without a change in receptive field shape. We also never observed large receptive field changes under control conditions where flies only experienced one cue in VR (not two cues) during the period between the receptive field mapping epochs (Fig. 5e, Extended Data Fig. 8 & 9).

By contrast, other E-PG neurons were essentially unmodulated by the fly’s heading during training (Fig. 5b, neuron 5). These neurons may reside in sectors of the ensemble that were “skipped over” by the bump during training. Interestingly, in these neurons, training had almost no effect on visual receptive fields (Fig. 5b, Extended Data Fig. 8). Overall, the

magnitude of heading modulation during training was significantly correlated with the subsequent visual receptive field change (Fig. 5f). This correlation implies that remapping depends on E-PG neuron activity. Simply exposing the fly to the altered visual environment is not sufficient; rather, visual cues must intersect with heading representations in E-PG neurons. Because R→E-PG synapses are the site of intersection between visual responses and heading representations, they are the most likely locus of plasticity. In a companion study, Kim et al.[22] used optogenetic manipulations to reach the same conclusion. Because R neuron dendrites form a retinotopic map which is fairly consistent across flies[5], it seems unlikely that the visual map in R neuron dendrites is experience-dependent, further supporting the notion that R→E-PG synapses are the locus of plasticity.

Discussion

We propose that correlated pre- and postsynaptic activity triggers associative long-term synaptic depression (LTD) of R→E-PG inhibition. This learning rule would explain why visual receptive fields and heading tuning are typically aligned in E-PG neurons. When an individual R neuron is activated by a visual cue, it should push the bump of activity toward the E-PG neurons it most weakly inhibits (Fig. 5g). If the full ring attractor network agrees with this outcome, then LTD will occur and those weak R→E-PG synapses will become even weaker, further reinforcing this outcome. To ensure network stability, LTD should be balanced by long-term potentiation (LTP) at R→E-PG synapses; the co-existence of LTD and LTP would also explain why we found bidirectional changes in visual receptive fields after training (Fig. 5b). These learning rules should produce a doubled pattern of R→E-PG synaptic weights after training in a two-cue world (Fig. 5g), reflecting the two-fold symmetry of visuomotor correlations.

The key result of this study – that visual inputs to E-PG neurons are plastic – supports theoretical models showing how a network can progressively establish a spatial map of the world by incorporating information about consistent sensory cues during exploration[7–12]. In robotics, this process is called simultaneous localization and mapping (SLAM)[23]. Our results provide direct experimental evidence for this type of unsupervised learning at the level of synaptic potentials *in vivo*.

In a simultaneous localization and mapping framework, visual cues are often local, meaning they can change in size and apparent angle as they are approached; by contrast, we chose to use visual cues which could not be approached, simplifying the relationship between heading and visual cues. This choice was motivated by the known receptive field properties of R2/4d neurons, which seem adapted to detect the position of the sun (or moon). Specifically, R2/4d neurons have large inhibitory surrounds, meaning they only respond robustly to isolated visual objects[5,24] like the sun. The sun is an ideal compass cue because it is effectively at infinity[25].

We propose that plasticity at R→E-PG synapses allows the position of the Sun to be flexibly associated with other compass cues, such as the pattern of linearly polarized light in the sky[26], sky-wide chromatic/intensity gradients[27,28], and wind[29,30]. In other insects, the E-PG network responds to multiple sorts of compass cues[31,32], and navigation behavior can

depend on arbitrary learned associations between compass cues[33–35]. In a companion study, Kim et al.[22] presented evidence in favor of the idea that plasticity could be used to learn a complex conjunction of visual objects; in the future, to test this idea, it will be interesting to see whether any complex scene can generate a progressively more stable heading representation (offset) during training. It will also be important to extend the approach we have taken here to simulate a more naturalistic virtual world, to study how multiple sorts of cues influence the behavior of this network and the organism.

Online Methods

Fly husbandry and genotypes

Unless otherwise stated, flies were raised on standard cornmeal-molasses food (New Brown 19L, Archon Scientific Inc.) in an incubator on a 12-hour/12-hour light:dark cycle at 25°C with humidity between ~50–70%.

All experiments with visual stimuli used flies with at least one wildtype copy of the *white* gene, and most electrophysiology experiments used flies with two copies of the wildtype *white* gene (as detailed below).

The experimenter was not blind to genotype because we did not use genetic perturbations; the exception is Figure 3c (Kir2.1 perturbation). For the Figure 3c data set collected for driver line *R20A02-Gal4* the experimenter was blind to genotype after the pilot phase; because Fig. 3c pilot data were indistinguishable from subsequent data, all data were ultimately pooled, and overall the experimenter was blind to genotype in 67% of these recordings. For the data set obtained using the driver line *R54E12-Gal4*, the experimenter was not blind to genotype because the experimental genotype was obtained at a lower-than expected (sub-Mendelian) frequency, making it impractical to blind the experimenter.

Genotypes of fly stocks used in each figure are as follows:

Figs. 1, 2, 5 and Extended Data Figs. 1–4, 8, 9: *P{20XUAS-IVS-mCD8::GFP}attP40 / P{20XUAS-IVS-mCD8::GFP}attP40; P{R60D05-Gal4}attP2 / P{R60D05-Gal4}attP2*

Fig. 3a: *P{20XUAS-IVS-mCD8::GFP}attP40 / P{20XUAS-IVS-mCD8::GFP}attP40; P{GawB}EB1 / +*

Fig. 3b, R2 activation: *w / +; P{R19C08-lexA}attP40/P{20XUAS-IVS-mCD8::GFP}attP40; PBac{13xLexAop2-IVS-Syn21-Chrimson::tdT-3.1}VK00005 / P{R60D05-Gal4}attP2*

Fig. 3b, R4d activation: *w/+; P{ R60D05-lexA}attP40/P{13XLexAop2-mCD8::GFP}attP40; P{20XUAS-CsChrimson-tdTomato}VK00005* / P{R12B01-Gal4}attP2* (*see transgenes section)

Fig. 3b, no ChR: *P{20XUAS-IVS-mCD8::GFP}attP40 / P{20XUAS-IVS-mCD8::GFP}attP40; P{R60D05-Gal4}attP2 / P{R60D05-Gal4}attP2*

For Fig. 3c and Extended Data Fig. 6 (Kir2.1 silencing, driver 1) : *+ / w; P{R60D05-lexA}attP40/P{13XLexAop2-mCD8::GFP}attP40; P{R20A02-Gal4}attP2 / P{UAS-Hsap\KCNJ2.EGFP}*

Fig. 3c and Extended Data Fig. 6 (Kir2.1 silencing, driver 2) : *+ / w; P{R60D05-lexA}attP40/P{13XLexAop2-mCD8::GFP}attP40; P{R54E12-Gal4}attP2 / P{UAS-Hsap\KCNJ2.EGFP}*

Fig. 3c and Extended Data Fig. 6 (UAS-only controls): *+ / w; P{R60D05-lexA}attP40/ P{13XLexAop2-mCD8::GFP}attP40; + / P{UAS-Hsap\KCNJ2.EGFP}3*

Fig. 3c and Extended Data Fig. 6 (Gal4-only controls): *+ / w; P{GMR60D05-lexA}attP40 / P{13XLexAop2-mCD8::GFP}attP40; + / P{R20A02-Gal4}attP2*

Fig. 3c and Extended Data Fig. 6 (Gal4-only controls): *+ / w; P{GMR60D05-lexA}attP40 / P{13XLexAop2-mCD8::GFP}attP40; + / P{R54E12-Gal4}attP2*

Fig. 4 and Extended Data Fig.7: + / *w; P{UAS-GCaMP6f}attP40 / +; P{R60D05-Gal4}attP2 / +*

Extended Data Fig. 1–4, 8, 9: same as Figs. 1, 2, and 5

Extended Data Fig. 5: Extended Data Fig. 5 genotypes: *R57C10-FLPG5.PEST; UAS(FRT.stop)myr::smGdP-HA, UAS(FRT.stop)myr::smGdP-V5, UAS(FRT.stop)myr::smGdP-FLAG / R20A02-Gal4, R57C10-FLPG5.PEST; UAS(FRT.stop)myr::smGdP-HA, UAS(FRT.stop)myr::smGdP-V5, UAS(FRT.stop)myr::smGdP-FLAG / R54E12-Gal4*

Origins of transgenic stocks

The following GMR Gal4 lines were obtained from the Bloomington Drosophila Stock Center (BDSC) and are described previously [37]: *P{R60D05-Gal4}attP2*, *P{R60D05-lexA}attP40*, *P{R19C08-lexA}attP40*, *P{R12B01-Gal4}attP2, P{R54E12-Gal4}attP2, P{R20A02-Gal4}attP2*, *P{GawB}EB1* was obtained from the BDSC and is described previously [38].

P{20XUAS-IVS-mCD8::GFP}attP40 was a gift from Barret Pfeiffer and Gerry Rubin and is described previously [39]. *P{13XLexAop2-mCD8::GFP}attP40* was obtained from the BDSC and is described previously [39]. *PBac{13xLexAop2-IVS-Syn21-Chrimson::tdT-3.1}VK00005* was a gift from Barret Pfeiffer and David Anderson and is described previously [40]. *P{20X-UAS-CsChrimson-tdTomato}VK00005* was a gift from John Tuthill who obtained it from Barret Pfeiffer. (Note that we have confirmed that this CsChrimson insert is on the third chromosome, but it may not be in *VK00005*, given recombination frequencies observed in our lab. We have confirmed that this insertion does generate tdTomato expression and light-evoked currents in Gal4+ cells.) *P{UAS-Hsap\KCNJ2.EGFP}7* was obtained from the BDSC and is described previously [41]. *P{UAS-GCamp6f}attP40* was obtained from the BDSC via Thomas Clandinin and is described previously [42].

Transgenes for MultiColor FlpOut were obtained from the BDSC and are described previously [43]; these are *w[1118] P{y[+t7.7] w[+mC]=GMR57C10-FLPG5.PEST}su(Hw)attP8; PBac{y[+mDint2],* and *w[+mC]=10xUAS(FRT.stop)myr::smGdP-HA}VK00005 P{y[+t7.7]*, and *w[+mC]=10xUAS(FRT.stop)myr::smGdP-V5-THS-10xUAS(FRT.stop)myr::smGdP-FLAG}su(Hw)attP1.*

Fly preparation and dissection

Newly eclosed virgin female flies were anesthetized on ice (electrophysiology) or CO_2 (imaging) and were collected ~3–10 hrs (electrophysiology) or 12–26 hrs (imaging) before the experiment. In some cases, to promote walking behavior, we deprived the flies of food (but not water) for ~3–10 hrs before the experiment, and experiments were performed around the fly's subjective evening (±2 hrs from light to dark switch, Zeitgeber time 12); this was done in Fig. 5 and in 72% of recordings in Fig. 2. In all other experiments, there was not circadian restriction and flies were kept on food until the dissection. At the beginning of each dissection, the fly was cold-anesthetized.

For electrophysiology experiments, the preparation holder consisted of flat titanium foil secured in an acrylic platform, with the foil oriented parallel to the horizontal body plane; the fly's head and body were gently pushed partway-through a hole in the foil. For E-PG neuron electrophysiology, the head was pitched forward so the posterior surface was roughly parallel to the foil and most of each eye was under the foil. For R neuron electrophysiology, the head was positioned in a more upright angle, and a 90° bend was made in the foil to maximize the area of the eyes that was under the foil. For imaging experiments, the preparation holder was inverted-pyramid-shaped and was CNC machined from black acrylic (Autotiv), and the head was pitched forward so that the posterior surface was oriented dorsally and most of the eye was under the holder. The fly was always secured in the holder with epoxy (Loctite AA 3972) cured using a brief (<1s) pulse of UV light (LED-200, Electro-Lite Co). Wings were sometimes repositioned or removed. After the dorsal head was covered in saline, a hole was cut in the head capsule and some trachea were removed to expose the brain area of interest. To reduce brain movement, muscle 16 was removed, the proboscis was removed (Figs. 1–3, 5) or glued (Fig. 4) and the esophagus was clipped or removed (Fig. 4). For electrophysiology, an aperture was made in the perineural sheath around the somata of interest either by ripping gently with fine forceps or by using suction from a patch pipette filled with external solution.

The external solution contained (in mM): 103 NaCl, 3 KCl, 5 N-tris(hydroxymethyl) methyl-2-aminoethanesulfonic acid, 8 trehalose, 10 glucose, 26 $NaHCO_3$, 1 NaH_2PO_4, 1.5 $CaCl_2$ and 4 $MgCl_2$, with osmolarity adjusted to 270–273 mOsm. External solution was bubbled with 95% O_2 and 5% CO_2 and reached a final pH of 7.3. External solution was continuously perfused over the brain during electrophysiology and prior to imaging.

Patch-clamp recordings

Patch pipettes were made from borosilicate glass (Sutter, 1.5mm o.d., 86 i.d.) using a Sutter P-97 puller. For E-PG recordings, the pipette was fire polished after pulling[44] using a

microforge (ALA Scientific Instruments) to achieve a final resistance of 8–15 MΩ. For R neuron recordings, pipettes (4–10 MΩ) were not fire polished. The internal solution contained (in mM): 140 potassium aspartate, 10 4-(2-hydroxyethyl)-1-piperazineethanesulfonic acid, 4 MgATP, 0.5 Na_3GTP, 1 ethylene glycol tetraacetic acid, 1 KCl, and 13 biocytin hydrazide. The pH was 7.3, and the osmolarity was adjusted to ~268 mOsm. To encourage walking, the external solution was heated prior to the experiment[45] to ~25–32°C; this was done for all recordings in Fig. 5, 65% of recordings in Fig. 2, and 42% of recordings in Fig. 1. All other recordings were performed using external solution at room temperature.

To obtain patch-clamp recordings under visual control, we used an Olympus BX51WI microscope with a 40× water-immersion objective. Neurons were identified as GFP+ using a Hg-lamp source (U-LH100HG, Olympus) with an EGFP-longpass filter (U-N41012, Chroma). For experiments where the fly was positioned over a foam ball, far-red light was delivered from a fiber-coupled LED (740nm, M740F2, Thorlabs) via a ferrule patch cable (200 μm Core, Thorlabs) plugged into a fiber optic cannula (1.25 mm SS ferrule 200 μm core, 0.22 NA, Thorlabs) glued to the recording platform, with the tip of the cannula ~1 cm behind the fly. In experiments without the ball, the brain was illuminated with 780 nm light via the microscope condenser, and after the recording was obtained, the condenser was lowered to prevent it from obscuring the fly's view of the visual panorama.

Recordings were obtained using an Axopatch 200B amplifier and a CV-203BU headstage (Molecular Devices). Voltage signals were low-pass filtered at 5 kHz prior to digitization and then acquired with a NiDAQ PCI-6251 (National Instruments) at 20 kHz. Liquid junction potential correction was performed *post hoc* by subtracting 13 mV from recorded voltages[46].

Two-photon calcium imaging

Imaging experiments were performed using a two-photon microscope with a moveable stage (Thorlabs Bergamo II) and a fast piezoelectric objective scanner (Physik Instrument P725) for volumetric imaging. For two-photon excitation, we used a Chameleon Vision-S Ti-Sapphire femtosecond laser tuned to 940 nm. Images were collected using a 20× 1.0 n.a. objective (Olympus). Emission fluorescence was filtered with a 525 nm bandpass filter (Thorlabs) and collected using a GAsP photomultiplier tube (Hamamatsu).

The imaging region was centered on the protocerebral bridge, which is the brain region where E-PG neuron axons terminate. For E-PG neurons, there is an orderly and stereotyped mapping from the location of the cell's dendrite to the location of its axon terminal in the protocerebral bridge[47]. Following refs. [3,4], we chose to image E-PG axons rather than dendrites because the axons are more superficial, and so more optically accessible. The imaging region was 256×128 pixels, and 8–12 slices deep in the z-axis (3–5 μm per slice), resulting in a 6–9 Hz volumetric scanning rate.

Volumetric z-scanning signals from the piezoelectric objective scanner were acquired simultaneously with analog output signals from the visual panorama and analog outputs from FicTrac via a NiDAQ PCI-6341 at 4 kHz. Two-photon calcium imaging data was

acquired using ScanImage 2018 (Vidrio Technologies) with National Instruments hardware provided by Vidrio (NI PXIe-6341).

Measurement of locomotion

In all cases except Fig. 3a–b, the fly stood on a 9-mm ball made of white foam (FR-4615, General Plastics) painted with black shapes. The ball floated above a plenum made of opaque ABS-like plastic (Figs. 1, 2, 3c, 5) or optically clear acrylic (Fig. 4) 3D-printed by Autotiv. Air was flowed into the plenum at the base and flowed out at the top in the semi-spherical depression that cradled the ball. The ball was illuminated by either an infrared LED (780nm M780L3, Thorlabs) with a ground glass diffuser (DG10–220-MD Thorlabs) (Figs. 1, 2, 3c, 5) or else a round board 36 IR red LED lamp (SODIAL) (Fig. 4). The movement of the ball was tracked at ~60–70 Hz using a video camera (Firefly MV FMVU-03MTM, Point Grey) fitted with a Computar Macro zoom 0.3X-1x, 1:4.5 lens (Figs. 1, 2, 3c, 5) or a Tamron 23FM08L 8 mm 1:1.4 lens (Fig. 4). In experiments where we used a 360° visual panorama (Fig. 4), the image of the ball was reflected to the camera using a mirror (Thorlabs broadband dielectric mirror, 750–1100 nm, BB1-E03) positioned below the ball. Machine vision software (FicTrac) converted the image of the ball to an estimate of the ball's position in all three axes of rotation[48]. FicTrac was modified to send real-time analog measurements of all three ball motion axes to a USB DAQ (USB-3101, Measurement Computing). For closed-loop experiments, the yaw position voltage signal was used to update the azimuthal position of the visual cues displayed on the panorama.

Visual panorama

Visual stimuli were presented using a circular panorama (IORodeo) composed of modular square panels[49]. Each square panel was an 8×8 array of LEDs (8×8 "pixels") that refresh at 372 Hz or faster[49]. In electrophysiology experiments, these LEDs were green (peak = 525 nm). In imaging experiments, these LEDs were blue (peak = 470 nm) to minimize overlap with GCaMP6f emission. The vertical edge of the panorama was positioned approximately aligned with the vertical location of the fly. A single pixel along the top of the arena subtended ~3.6–3.7° of the fly's visual field; this range of 0.1° is due to the fact that individual pixels within each flat 8×8 array have slightly different distances from the fly's eye. A single pixel at the bottom of the arena subtended ~2.7°. These differences in pixel size were not compensated for in our experiments.

In Figs. 1, 2, 3c, and 5, we used a panorama composed of 9×2 panels. It spanned 270° azimuth and was oriented slightly asymmetrically so that it covered the azimuthal range from 127° left of the midline to +143° right of the midline. In Fig. 3a, we used a panorama composed of 6×2 panels that spanned 180° azimuth. In Fig. 4, we used a panorama composed of 12×2 panels that spanned 360° azimuth. All visual panoramas were the same height and spanned ~43° vertically within the fly's visual field.

In electrophysiological experiments, to reduce electrical noise, the panorama was wrapped with grounded copper mesh that was colored with a black marker to reduce reflections. To further reduce reflections, the front surface of each panel was covered with a diffuser (SXF-0600 Snow White Light Diffuser, Decorative Films®). In imaging experiments,

instead of diffuser film, we used tracing paper as a diffuser, and four layers of filters (Rosco R381,bandpass center 440, FWHM 40 nm) were used to minimize detection of the visual stimulus by the GCaMP6f emission collection channel.

Open- and closed-loop modes of visual stimuli

To map visual receptive fields, we used a bright vertical bar (2 pixels wide, 7°) that spanned the full height of the panorama (~43°). The bar was flashed for 500 ms followed by 500 ms of darkness. During open-loop mode the display updated at 50 Hz. The bar was presented in a pseudorandom order at 35 different evenly-spaced azimuthal positions across the screen (−120° to 135°). During each open-loop epoch, each bar position was used 4–5 times in total. For R neuron recordings, fewer positions were used (27 positions, −139° to 56°) and each location was used 5–6 times in total.

To map heading tuning curves and to provide visuomotor training (closed-loop mode), we used a visual panorama containing either one vertical bar (“1-cue”) or else two bars positioned on opposite sides of the virtual world (“2-cue”). Each vertical bar was identical to the bar we presented in open-loop mode. In closed-loop mode, we controlled the azimuthal position of the visual pattern using the yaw-position voltage output from FicTrac. Between consecutive closed-loop epochs there were 3–40 secs of darkness, after which we shifted the pattern randomly (Fig. 4) or else by a variable 45° or 90° increment (Fig. 2, 5) before returning to closed loop. Analog output signals from the visual panel system and from FicTrac were digitized with a NiDAQ PCI-6251 (National Instruments) at 20 kHz (electrophysiology) or with a NiDAQ PCI-6341 (National Instruments) at 4 kHz (calcium imaging). In Fig. 4, the 360° yaw output signal was mapped directly to the 360° visual panorama. In Figs. 2 and 5, we needed to use a 270° panorama due the space constraints imposed by the electrophysiology set-up, and so the 360° yaw output signal was mapped linearly to the 270° panorama so that objects did not disappear when they reached one edge of the panorama but instead moved immediately across the gap[1]. Thus, for example, whenever the fly made a 20° fictive right turn, the visual pattern would move 15° left. The exception to this is whenever the bar passed through the 90° gap; here the bar traversed the gap immediately, as if the gap did not exist. How often this jump occurred varied from fly to fly depending on walking speed. We estimate that our most active flies experienced these 90° jumps of the cue ~ 10 times per minute during a typical 1-cue closed-loop trial. Note that in the 270° panorama, the 2-cue pattern contained two bars spaced 135° apart.

In pilot electrophysiology recordings, during closed-loop epochs, the 360° yaw output signal was mapped to 360° of visual space (rather than 270°). This meant that the visual cue was only displayed when it resided on the 270° panorama, and the cue simply disappeared when it moved into the 90° sector where the panels were missing. The heading tuning data from these 16 recordings is not included in the final dataset, but some open-loop visual responses from these neurons are included in Fig. 1g. We did not observe any systematic differences in the open-loop visual responses of these neurons from pilot recordings.

Optogenetic stimulation

Chrimson[50]-expressing flies were raised on cornmeal-agar medium supplemented with rehydrated potato flakes (Carolina Biological Supply) mixed with 100 μL of all-trans-retinal stock solution (Sigma; 17 mM in ethanol). Fly vials were wrapped in foil to prevent photo-conversion of the all-trans-retinal. Controls in Fig. 3b were raised on molasses food without all-trans-retinal. For optogenetic stimulation, we used the Hg-lamp source (U-LH100HG) to deliver a 5-ms pulse of green light (530–550nm, 2–4 mW, TRITC-Cy3 filter cube, Chroma) via the objective. A shutter (Uniblitz Electronic) controlled the pulse duration.

Experimental epoch structure

Each open-loop epoch always lasted 150 secs and consisted of a sequence of random cue flashes. Each closed-loop epoch lasted 4 min (Figs. 2 and 5) or 2 min (Fig. 4), during which time the visual pattern was continuously present and rotated in proportion to the fly's fictive yaw velocity.

In Fig. 1., open-loop epochs were usually interleaved with 4-min 1-cue closed-loop epochs, although occasionally two open-loop epochs were delivered consecutively.

In Fig. 2., at least one 4-min 1-cue closed-loop epoch was presented prior to obtaining a recording, and after the recording was obtained, open-loop epochs and 4-min 1-cue closed-loop epochs were interleaved.

In Fig. 3c, only open-loop epochs were presented.

In Fig. 4, for pre-training, we presented at least five 2-min 1-cue closed-loop epochs. For training, we presented 10 2-min 2-cue closed-loop epochs. For post-training, we presented at least two 2-min 1-cue closed-loop epochs.

In Fig. 5., 1–6 epochs of 1-cue closed-loop experience were presented prior to obtaining an E-PG neuron recording. Once the recording was obtained, the epoch structure was as follows. First, for pre-training, we cycled through 4-min 1-cue closed-loop epochs alternating with open-loop epochs, for a total of 2–6 cycles. For training, we presented three consecutive 4-min 2-cue closed-loop epochs (experimental condition) or three consecutive 4-min 1-cue closed-loop epochs (matched control condition). For post-training, we presented one open-loop epoch. This protocol was followed in all training experiments in Fig. 5, with two exceptions. In one case, pre-training consisted of an open-loop epoch, followed by a closed-loop epoch, followed by another open-loop epoch (i.e., 1.5 cycles through the normal pre-training procedure). In the other case, during the closed-loop epochs prior to obtaining the recording, the fly experienced a different visual pattern consisting of sparse randomly-distributed single pixels (a "star field" pattern), and this fly also received two consecutive open-loop epochs (instead of one) during pre-training.

Immunohistochemistry

MultiColor FlpOut (MCFO): In Extended Data Fig. 5, MCFO was used to identify the morphological types of R neurons labeled by *R20A02-Gal4*. MCFO immunostaining was performed essentially as described in ref. [43]. Primary incubation solution contained mouse

anti-Bruchpilot antibody (1:30, Developmental Studies Hybridoma Bank, nc82), rat anti-FLAG (1:200, Novus Biologicals), rabbit anti-HA (1:300, Cell Signaling Technologies), and 5% normal goat serum (NGS) in PBST. Secondary incubation solution contained Alexa Fluor 488-conjugated goat anti-rabbit (1:250, Invitrogen), ATTO 647-conjugated goat anti-rat (1:400, Rockland), and Alexa Fluor 405-conjugated goat anti-mouse (1:500, Invitrogen) and 5% NGS in PBST. Tertiary incubation solution contained DyLight 550-conjugated mouse anti-V5 (1:500, Bio-Rad) and 5% normal mouse serum in PBST.

visualization of biocytin-filled neurons: Brains containing biocytin-filled neurons were processed after electrophysiological recording using standard procedures. Primary incubation solution contained mouse anti-Bruchpilot antibody (1:30, Developmental Studies Hybridoma Bank, nc82), chicken anti-GFP (1:1000, Abcam), Alexa Fluor 568-conjugated streptavidin (1:1000, Invitrogen), and 5% NGS in PBST. Secondary incubation solution contained Alexa Fluor 488-conjugated goat anti-chicken (1:250, Invitrogen), Alexa Fluor 633-conjugated goat anti-mouse (1:250, Invitrogen), Alexa Fluor 568-conjugated streptavidin (1:1000, Invitrogen), and 5% NGS in PBST.

confocal microscopy and image analysis: Brains processed for MCFO were imaged using an Olympus FV1000 confocal microscope. Series of between 50 and 100 optical sections (1.0-μm spacing) were imaged using either a UPLFLN 40× oil-immersion lens (n.a. 1.3) or a PLAPON 60× oil-immersion lens (n.a. 1.42). R neuron MCFO clones were classified into 11 subtypes following ref. [6] based on the consensus of two experts. Maximum intensity z-projection were rendered and adjusted using cropping and thresholding tools in Fiji (ImageJ), and assembled into figures using Illustrator (Adobe).

Confocal microscopy of brains processed for biocytin fills, or to assess expression of Kir2.1-EGFP within R neurons (Fig. 3), was performed using a Leica SP8 or Leica SPE equipped with a 40x oil-immersion lens (n.a. 1.3). Cell body counting of EGFP-labeled R neurons was performed independently by two experts using the Fiji Cell Counter plugin[51], and the mean count for each brain hemisphere is reported (Extended Data Fig. 6).

Data analysis

E-PG neuron visual receptive fields: in Figs. 1g, 2c, 3c, and 5b (and Extended Data Figs. 1–4, 8, 9), visual responses were calculated by taking the mean voltage during the final 250 ms of the 500-ms cue flash, and subtracting the mean voltage during the 250 ms preceding the flash, averaged over all presentations of the cue at each position. For display, visual receptive field curves were often smoothed using a median filter with a width of 3 cue positions (Fig. 1g, 3c, Extended Data Fig. 2) or 2 cue positions (Fig. 2c, 5b, Extended Data Fig. 3, 4, 8, 9). Peak visually-evoked hyperpolarization (Fig. 3c) and mean visually-evoked hyperpolarization (Extended Data Fig. 6) were calculated on the median filtered tuning curves.

E-PG neuron heading tuning: In Figs. 2 and 5 (and Extended Data Figs. 3, 4, 8 and 9), heading tuning curves were calculated by first binning heading into 35 bins centered on the visual cue positions. The voltage trace was filtered using a median filter with a width of 40

ms to remove spikes, and the mean filtered voltage was measured for each heading during an epoch. For heading tuning curves calculated from multiple epochs, the voltage measurement for each heading bin was weighted relative to the number of samples in each individual epoch and the mean was then taken across epochs. For display, heading tuning curves were often smoothed using a median filter with a width of 2 cue positions (Fig. 2c, 5b, Extended Data Figs. 3, 4, 8 and 9).

yaw during open-loop epochs: In Fig. 1e, the FicTrac yaw position signal was unwrapped, converted into radians, low-pass filtered (Butterworth) at 25 Hz, and differentiated to obtain angular velocity. On rare occasions, a value >2500°/s occurred in an isolated time sample, likely due to imperfect nature of the unwrapping-and-differentiation procedure; these values were replaced with the value of the preceding sample. In Fig. 1f, the time-averaged yaw velocity was calculated by taking mean yaw position during the final 250 ms of the flash and subtracting mean yaw position during the 250 ms directly preceding the flash, and then dividing by the elapsed time (500 ms). We averaged data from left and right versions of the same cue displacement (because it seemed unlikely that a large group of flies would show a systematic bias in the right or left direction) in order to obtain mean yaw velocity responses to a total of 16 cue positions for each of 73 flies, thus obtaining 73×16 data points. We took the mean across flies at each cue position and plotted this as the black line in Fig. 1f. Next, to model the null case (where visual cue position has no effect), we randomly drew 73 values (with replacement) from the matrix, without regard for cue position or fly identity, and we calculated the mean of these 73 values; we constructed a bootstrap distribution by repeating this procedure 10,000,000 times, each time calculating the mean of 73 randomly-drawn values. This bootstrap distribution was used to obtain a 95% confidence interval, which was then adjusted for multiple comparisons using a Bonferroni correction (m=16 tests). None of the true mean values (black) were outside this adjusted confidence interval (magenta lines). Extended Data Fig. 1e used the same procedure except that the independent variable was the distance of the cue jump rather than the position of the cue. Finally, as a further control, we also examined whether any individual flies had a significant yaw velocity response to any cue position (Extended Data Fig. 1d). Because individual flies might be right- or left-handed[52], we did not average data from right and left cue positions in this analysis; thus there were 35 cue positions. For each fly, we computed trial-averaged yaw velocity for each of 2–8 open-loop epochs, and we created a matrix containing all cue positions for every epoch in that fly's data set. We then randomly drew a number of values (with replacement) from the matrix (number of epochs × 35 cue positions) to match the number of epochs we actually recorded for that fly. This procedure randomized with respect to cue position and epoch number. For each fly, a bootstrap distribution was obtained by repeating this procedure 100,000 times, each time calculating the mean of the drawn values. The difference between the observed trial-averaged yaw responses for each cue position and the mean of the bootstrap distribution was used to obtain a p-value (two-sided). In this manner, a p-value was calculated for every fly at every cue position (73×35 p-values). The statistical significance of each trial-averaged yaw was assessed for each fly and each position at an alpha level of 0.05 using the Bonferroni-Holm method to correct for multiple comparisons. No tests showed a statistically significant yaw velocity for any individual fly at any cue position.

correlations between visual receptive fields and heading turning curves in E-PG neurons: In Fig. 2c–d, heading tuning curves and visual receptive fields were smoothed using a median filter with a width of 2 cue positions. Correlation coefficients were computed on smoothed curves (40 pairs in total). In Fig. 2d, as a control, we randomly drew (with replacement) 40 heading tuning curves and 40 visual response curves, yielding 40 correlation coefficients. The mean of that correlation value was then recorded. This process was repeated 10,000,000 times to build a bootstrap distribution, and the 95% confidence interval of this distribution was computed.

R neuron visual receptive fields: In Fig. 3a, spikes were detected after low-pass filtering the recorded current at 1 kHz by identifying deflections >15 pA that occurred outside a 0.5-ms refractory period. Spike rate was measured over the 500-ms visual stimulus period.

E-PG response to R neuron optogenetic stimulation: In Fig. 3b, peak hyperpolarization was calculated as the trial-averaged voltage during a 1-sec baseline period minus the minimum trial-averaged voltage reached in the 1 sec following the 5-ms optogenetic stimulus. Four optogenetic stimulus trials were recorded per cell.

E-PG ensemble representations of heading direction: In Fig. 4, rigid motion correction in the *x*, *y*, and *z* axes was performed for the volumetric imaging stacks for every epoch using the NoRMCorre algorithm[53]. This algorithm performs piece-wise rigid registration of small overlapping sectors within the field of view, and then merges the sectors via interpolation, allowing approximate cancellation of non-rigid brain movement artifacts. Motion correction was parallelized on a high-performance computing cluster. For each epoch, we defined 16 regions of interest (ROIs) corresponding to the 16 glomeruli in the protocerebral bridge; each ROI was defined in one *z*-plane. To calculate the time-dependent change in fluorescence (ΔF/F) for each glomerulus, we used a baseline fluorescence (F) defined as the mean of the lowest 5% of raw fluorescence values across the entire experiment for that glomerulus. We excluded from the baseline the rare frames that were lost as a result of the rigid motion correction algorithm. The singular “bump” of activity in E-PG dendrites within the ellipsoid body[1] translates into two bumps in the protocerebral bridge[3,4]; these two bumps move together, so that the signal has a spatial period of 8 glomeruli in the protocerebral bridge. Therefore, to calculate the neural representation of heading direction, we took the spatial Fourier transform of ΔF/F in the protocerebral bridge across all 16 glomeruli, and we used the phase of the Fourier component at 8 glomeruli as the phase of the neural representation of heading for each time point; this procedure follows that of ref. [3]. We used the sign convention whereby a positive change in phase corresponds to a rightward movement of the bumps in the protocerebral bridge, and a clockwise movement of the bump in the ellipsoid body (when viewed from the posterior side of the brain). For display purposes only, in Fig. 4a, we averaged together the ΔF/F signals from the right and left half of the protocerebral bridge (which is why only one bump is visible); this averaging was not performed as part of the data analyses described above.

offset of the E-PG ensemble reference frame: In Fig. 4c–d, to calculate the offset of the reference frame (the difference between the fly's heading and the neural representation of heading), we first downsampled the behavioral data to match the volumetric imaging rate (6–9 Hz).We removed time points in which the FicTrac analog signals were problematic or when the power of the Fourier transform was below a specified threshold (0.1). We also excluded the first 3 secs of each 2-min closed-loop epoch due to a delay between imaging trigger and the start of the visual stimulus. We then took the angular position of the visual panorama from the analog voltage output of the LED panel system (positive defined as to the right of the fly, or clockwise when viewed from above the setup). We calculated the offset of the E-PG ensemble reference frame as the negative of the spatial Fourier transform phase minus the position of the visual panorama. This value is consistent with methods used in ref. [3] to calculate the offset between the bump position in the protocerebral bridge and the ball yaw position.

effect of training on visual receptive fields: In Fig. 5 (and Extended Data Figs. 8–9), heading tuning curves and visual receptive fields were smoothed using a median filter with a width of 2 samples (cue positions). The last pre-training open-loop epoch (probe 1) and the first post-training open-loop epoch (probe 2) were used for the following analyses. In Fig. 5d–f, "absolute change" was obtained by subtracting the two visual receptive fields (Δ=post–pre), then summing the absolute value of Δ over all cue positions, and finally dividing by the number of positions. In Fig. 5d, "change in receptive field shape" was obtained by cross-correlating probe 1 and probe 2 and taking ($1-R^2$). In Fig. 5f, "modulation by heading during turning" was taken as the difference between the maximum and the minimum of the heading direction turning curve.

controls for training: In Fig. 5e, to estimate the drift in visual receptive field under control conditions, we had flies navigate in a 1-cue world (rather than a 2-cue world) during the waiting period between the open-loop epochs. In some cases ("matched control" in Extended Data Fig. 9), flies received exactly the same protocol as the experimental condition except with 1-cue closed-loop during the training period; in other words, these matched controls received 12 consecutive minutes of 1-cue (rather than 2-cue) closed-loop during the "training" period. For other controls ("control" in Extended Data Fig. 9) we identified experiments from Fig. 2 where the recording had lasted long enough for us to present 4 open-loop epochs interleaved with 4 1-cue closed-loop epochs. In these recordings, the 2^{nd} and 4^{th} open-loop epochs were separated by > 12 min (typically ~15 min) and so they are appropriate controls for the training protocol. We therefore treated the 2^{nd} and 4^{th} open-loop epochs as if they were "probe 1" and "probe 2" epochs in a training experiment, and we analyzed them as described above for the true training experiments. The important distinction is that this second group of control flies experienced 1-cue rather than 2-cue closed-loop epochs during the window between probe 1 and probe 2.

Data inclusion

Figs. 1 & 2: Epochs were included if the cell was healthy; specifically, this meant that the epoch-averaged voltage was below −33 mV and within 15 mV of the voltage observed at the start of the first epoch of the experiment, and also if the spike amplitude was >50% of the

amplitude observed in the first epoch. Closed-loop epochs were included if the fly visited all heading directions during that epoch. Cells were included if ≥2 open-loop epochs met these criteria; in Fig. 2 we also required that ≥2 closed-loop epochs met these criteria.

Fig. 3: Cells were included if ≥2 open-loop epochs met our cell health criteria. A single recording from the *UAS/+* control genotype was excluded because the biocytin fill showed that it was not an E-PG neuron. All other biocytin-filled neurons analyzed during this project (i.e., 65 of 66 neurons) were confirmed to be E-PG neurons. All recordings that were not imaged *post hoc* were therefore assumed to target E-PG cells.

Fig. 4: 5/24 flies were excluded due to either weak fluorescence or an unstable offset between the angle of the E-PG bump and the fly's heading angle at the end of the initial closed-loop 1-cue epoch.

Fig. 5: Cells were included if the epoch-averaged voltage from all epochs of the experiment (pre-training, training, post-training) was <−33 mV, and if the fly visited all heading directions during the 2 epochs (8 min) of 1-cue closed-loop prior to training and during the final 2 epochs (8 min) of 2-cue closed-loop training. We required that the fly's mean yaw velocity was >20°/s during the final 2 epochs of the 2-cue closed-loop training; 10 cells were excluded due to this restriction. We also removed recordings where the visual receptive field and/or heading turning curve were almost flat during the pre-training period (max-min ≤2mV); 6 cells were removed due to this restriction.

On occasion, during E-PG neuron electrophysiological recordings, we observed unexpected large inhibitory postsynaptic potentials with a stereotyped sharp onset, a large amplitude (>15mV), and a stereotyped time course. They were followed by a prolonged period of depolarization when the variance of the voltage trace was also diminished. These events interfered with visual and heading tuning measurements, and so for Figs. 1–3, any epoch where such an event occurred was excluded from the analysis. For Fig. 5, the event was clipped but the rest of the epoch was used; 5% of open loop epochs and 10% of closed-loop epochs were clipped in this manner.

Analysis was performed using Matlab R2016b, R2017a, and R2017b (MathWorks).

Determination of sample sizes

For genetic perturbation experiments (Fig. 3c), the number of experiments performed was determined by first collecting a pilot data set of (n=4 for the 3 genotypes using the *R20A02-Gal4* driver line). Based on the initial effect size, power analysis was used to determine the number of experiments needed to test the hypothesis that visually-evoked hyperpolarization was smaller in the experimental genotype. For all other experiments, sample sizes were chosen based on standard sample sizes in the field.

Extended Data

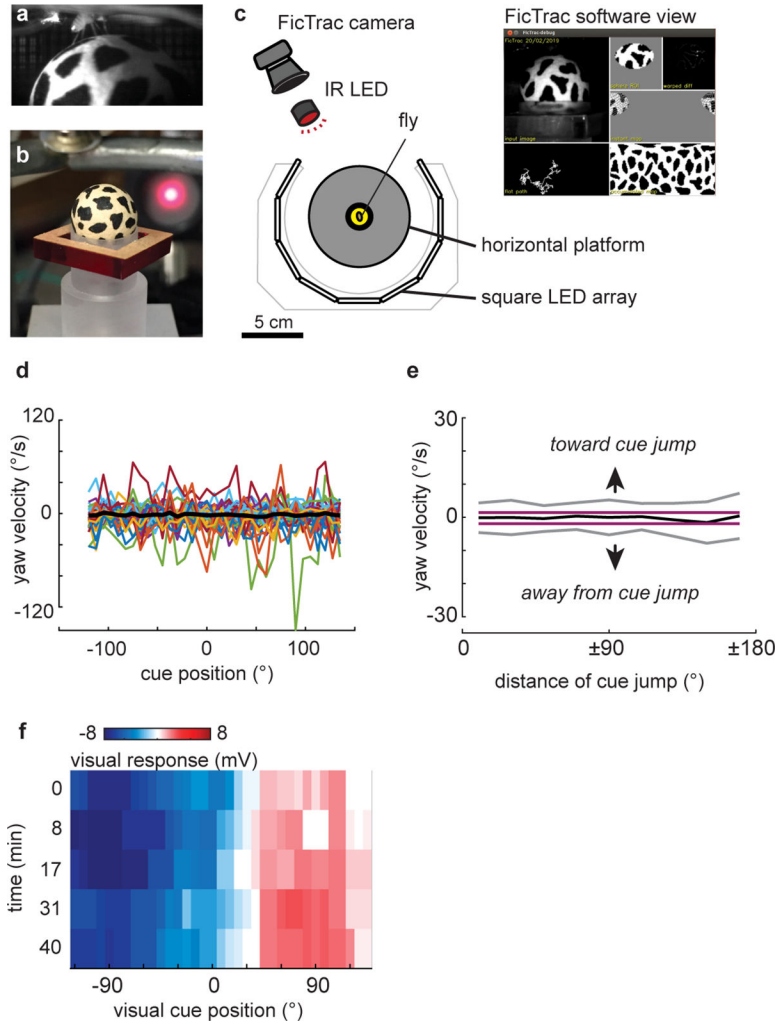

Extended Data Fig. 1: Measuring behavior and E-PG visual responses.

a. Side view of a fly walking on an air-cushioned ball during an electrophysiology experiment.

b. Image of the ball and plastic holder. Air flows up through the holder and out the semi-spherical depression that cradles the ball.

c. Schematic of the experimental set-up viewed from above. The fly is secured in an aperture in the center of a horizontal platform. The platform is surrounded by a circular panorama. The panorama is composed of square LED arrays[49] (2 squares vertically × 12 squares horizontally). The ball is illuminated by an infrared (IR) LED which is visible as a red spot in (b). A camera captures an image of the ball to enable tracking using FicTrac[48]. Inset shows FicTrac view. Camera and IR LED are not drawn to scale.

d. Fly's yaw velocity versus cue position. This is the data set that is the basis for Fig. 1f, but here broken down into individual-fly-averages, and with right (+) and left (−) cue positions kept separate. Positive velocities are right turns, and negative velocities are left turns. No tests showed a statistically significant yaw velocity ($p<0.05$, two-sided comparison to

bootstrap distribution) for any individual fly at any cue position. For details of analysis, see Methods: yaw during open-loop epochs.

e. Yaw velocity in response to the visual cue presentation. This analysis is the same as that shown in Fig. 1f, but here yaw velocity is plotted versus the distance of the cue jump between consecutive trials. As in Fig. 1f, we show mean (black) ± 1 standard deviation (gray) across experiments (73 experiments in 68 flies). Magenta lines show the bootstrapped 95% confidence interval of the mean across flies after randomizing cue positions, Bonferroni-corrected for multiple comparisons. Because the mean lies within these bounds, it is not significantly different from random. This analysis further supports the conclusion that there is no systematic yaw response to the random flashes of the vertical bar. For details of analysis, see Methods: yaw during open-loop epochs.

f. The visual receptive field of an example cell measured multiple times over the course of a 40-min recording. Each row shows data from a separate visual mapping epoch. Data from this example cell are also shown in Fig 1e. Note the stability of the visual receptive field over this time period.

Extended Data Fig. 1 genotype: *UAS-mCD8::GFP / UAS-mCD8::GFP; R60D05-Gal4 / R60D05-Gal4*

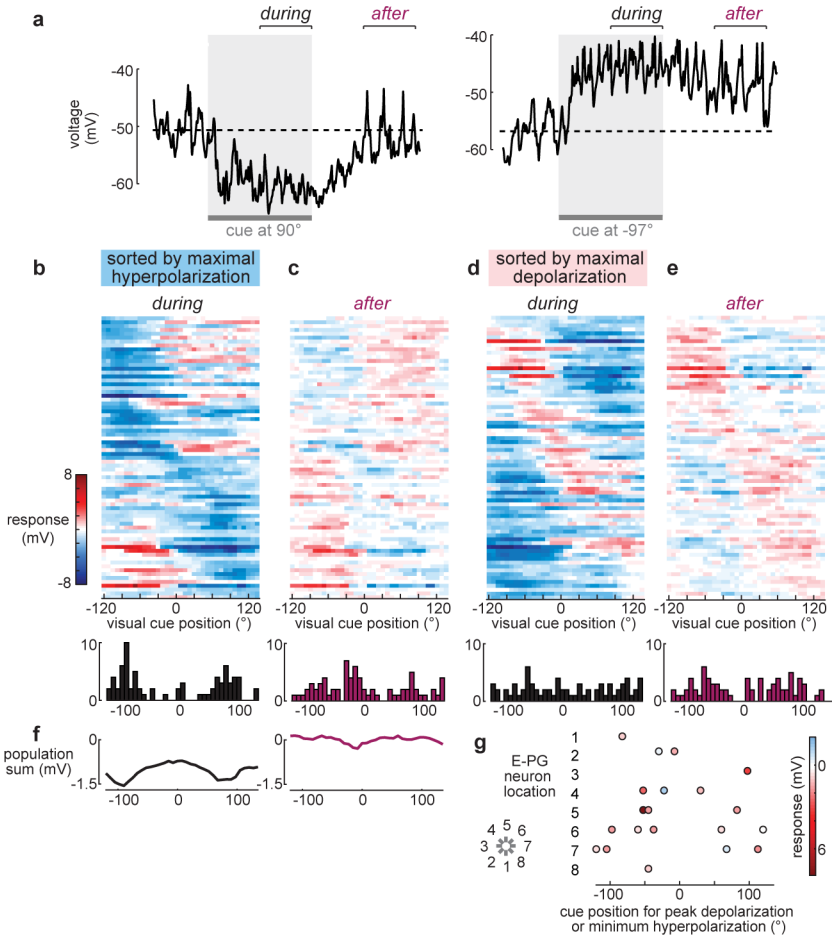

Extended Data Fig. 2: Visually evoked hyperpolarization and depolarization, during and after cue presentation.

a. Example voltage responses of the same E-PG neuron to two cue positions. Dashed lines indicate the mean baseline voltage before the cue. This neuron is hyperpolarized by the cue at 90° and depolarized by the cue at −97°. Note that hyperpolarization decays more rapidly than depolarization. In (b), to quantify visual receptive fields, we measured the change in voltage ***during*** cue presentation and ***after*** cue removal in the 250-ms windows marked here with brackets, in both cases relative to baseline.

b. Summary of E-PG visual receptive fields measured ***during*** cue presentation. Cells are sorted by the cue position that evokes maximal hyperpolarization. The histogram below shows the number of E-PG neurons with maximal hyperpolarization at each cue position (73 E-PG neurons in 68 flies).

c. Summary of E-PG visual receptive fields measured ***after*** cue removal. Cell order is the same as in (b). Note that hyperpolarizing responses tend to decay, whereas depolarizing responses tend to persist; this is consistent with the hypothesis the hyperpolarization during cue presentation is due to direct synaptic inhibition from R neurons, whereas depolarization is polysynaptic and caused by withdrawal of tonic synaptic inhibition. The histogram below shows the number of E-PG neurons with maximal hyperpolarization ***after*** cue removal for each cue position.

d. Same as (b), but sorted by the cue position that evoked maximal depolarization (minimal hyperpolarization), as in Fig. 1g.

e. Same as (c), but with the cell order as in (d).

f. Summed response across all neurons measured during (left) and after (right) the cue. The left curve has a pair of minima around ~±100°; this bias is likely inherited from R neuron receptive fields, which are biased toward positions offset from the visual midline[5]. By contrast, the right curve is relatively flat.

g. Visual cue position eliciting maximal depolarization (minimum hyperpolarization), plotted versus E-PG neuron location, for the 21 recorded E-PG neurons that were filled. No signification correlation was observed (circular correlation coefficient = −0.15, p = 0.49)[36].

Extended Data Fig. 2 genotype: *UAS-mCD8::GFP / UAS-mCD8::GFP; R60D05-Gal4 / R60D05-Gal4*

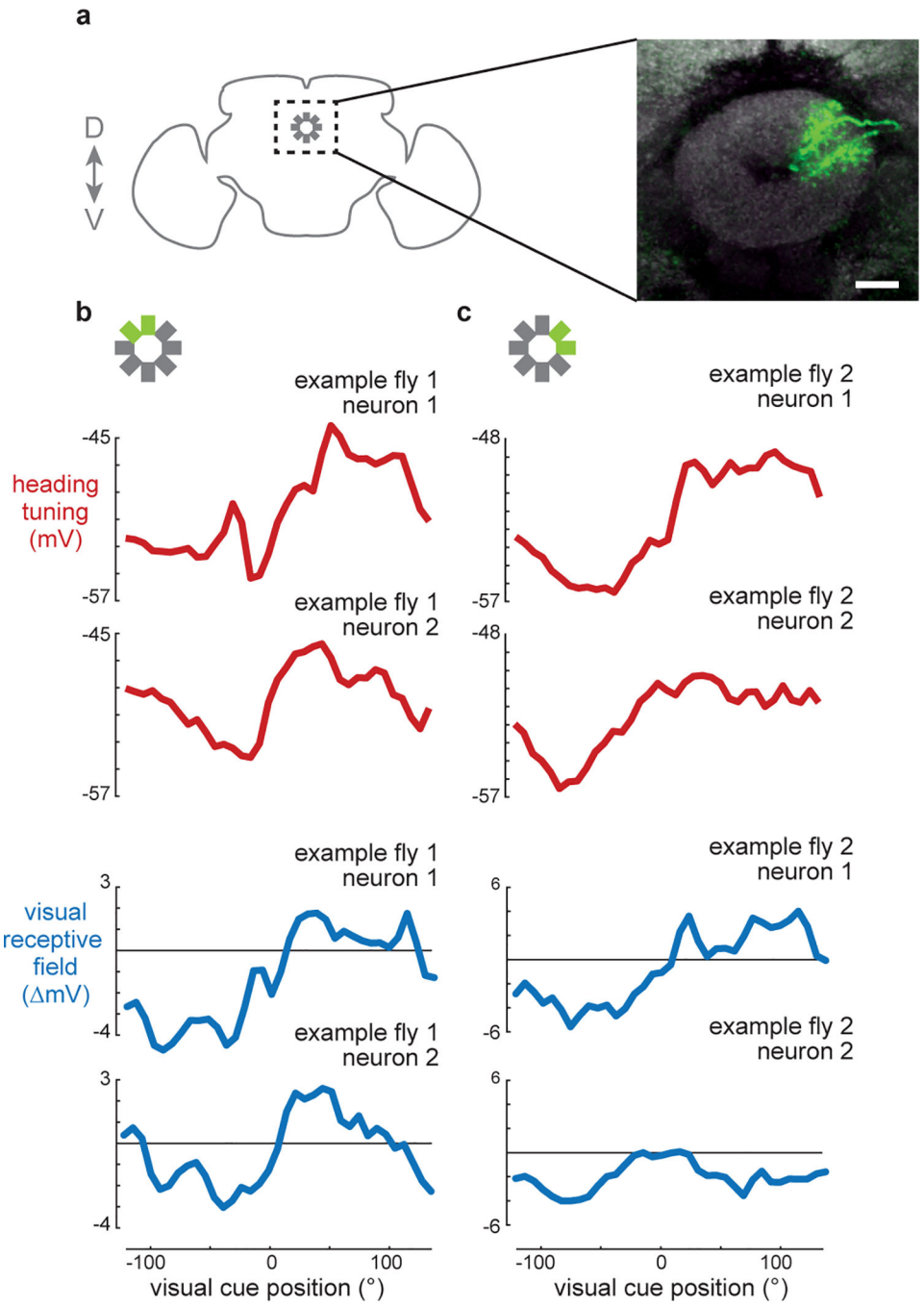

Extended Data Fig. 3: E-PG neuron pairs recording sequentially from the same brain.

a. Two biocytin-filled dendrites (green) from sequentially recorded E-PG neurons that innervate adjacent wedges within the ellipsoid body. Neuropil reference marker is shown in gray (anti-nc82 antibody). Images are maximum intensity z-projections. Scale bar is 10 μm. The schematic shows the approximate position of ellipsoid body and E-PG dendrites from a coronal view of the fly brain.

b-c. Heading tuning (red, measured in virtual reality) and visual receptive field (blue, measured with random flashes) from sequentially recorded E-PG pairs from two example

flies. Dendritic locations of the recorded neurons are green in the ellipsoid body schematic above each set of plots. In both cases, by chance, the two dendrites were physically adjacent. In both cases, adjacent E-PG neurons from the same fly exhibited similar visual receptive fields and heading tuning curves, supporting the conclusion that adjacent E-PG cells typically receive inhibition from adjacent regions of visual space and represent adjacent heading directions. Comparing the visual receptive field and the heading tuning curve for each neuron yielded correlation coefficients (Pearson's) of 0.76 (fly 1 neuron 1), 0.90 (fly 1 neuron 2), 0.95 (fly 2 neuron 1), and 0.65 (fly 2 neuron 2).

Extended Data Fig. 3 genotype: *UAS-mCD8::GFP / UAS-mCD8::GFP; R60D05-Gal4 / R60D05-Gal4*

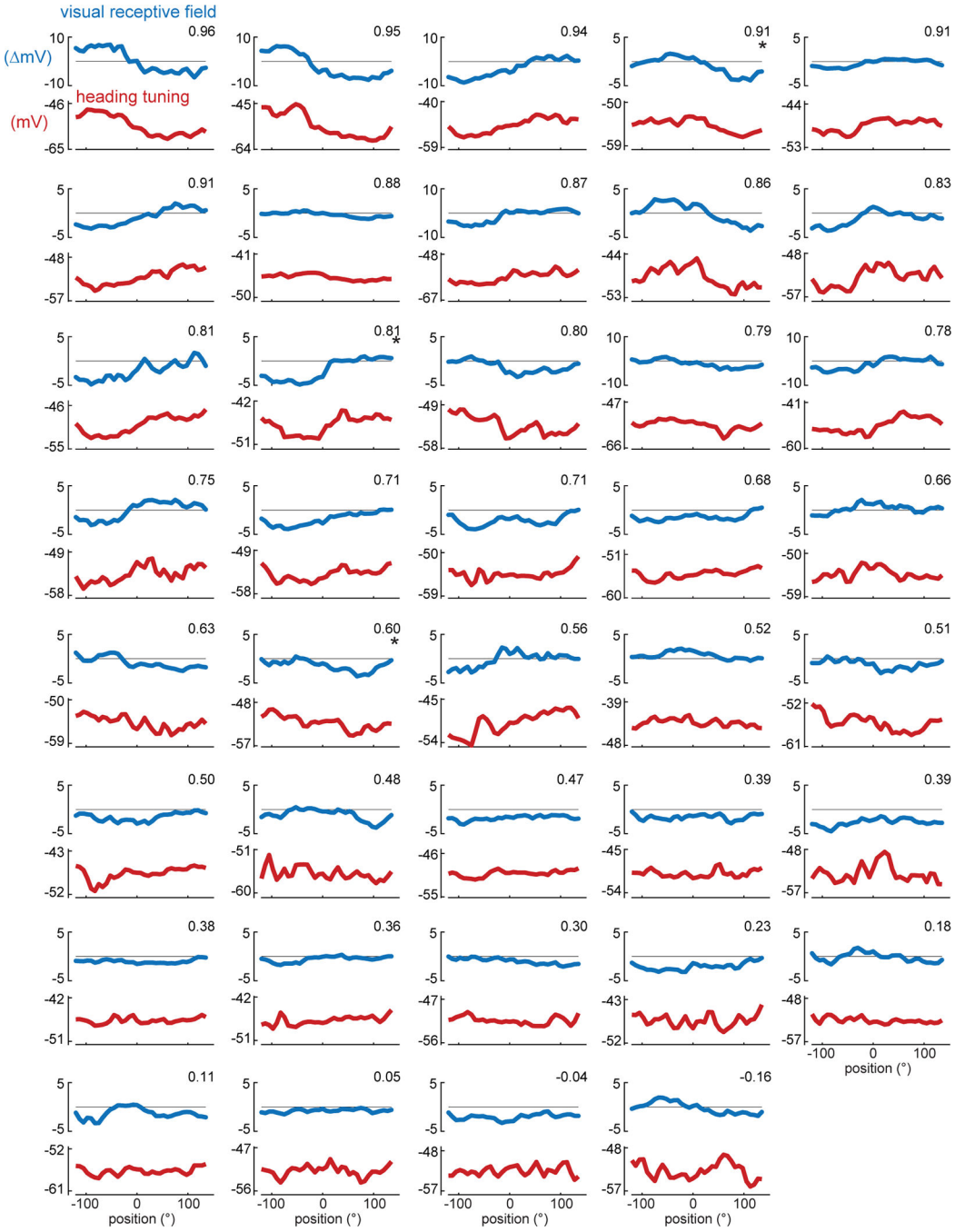

Extended Data Fig. 4: E-PG neuron visual receptive fields and heading tuning.

Heading tuning (red, closed-loop mode) and visual receptive fields (blue, open-loop mode) for all 40 recorded E-PG neurons (from 39 flies). For each neuron, the correlation coefficient (Pearson's) is reported for the comparison between the visual receptive field and the heading tuning curve. Asterisks denote data also shown in Fig. 2.

Extended Data Fig. 4 genotype: *UAS-mCD8::GFP / UAS-mCD8::GFP; R60D05-Gal4 / R60D05-Gal4*

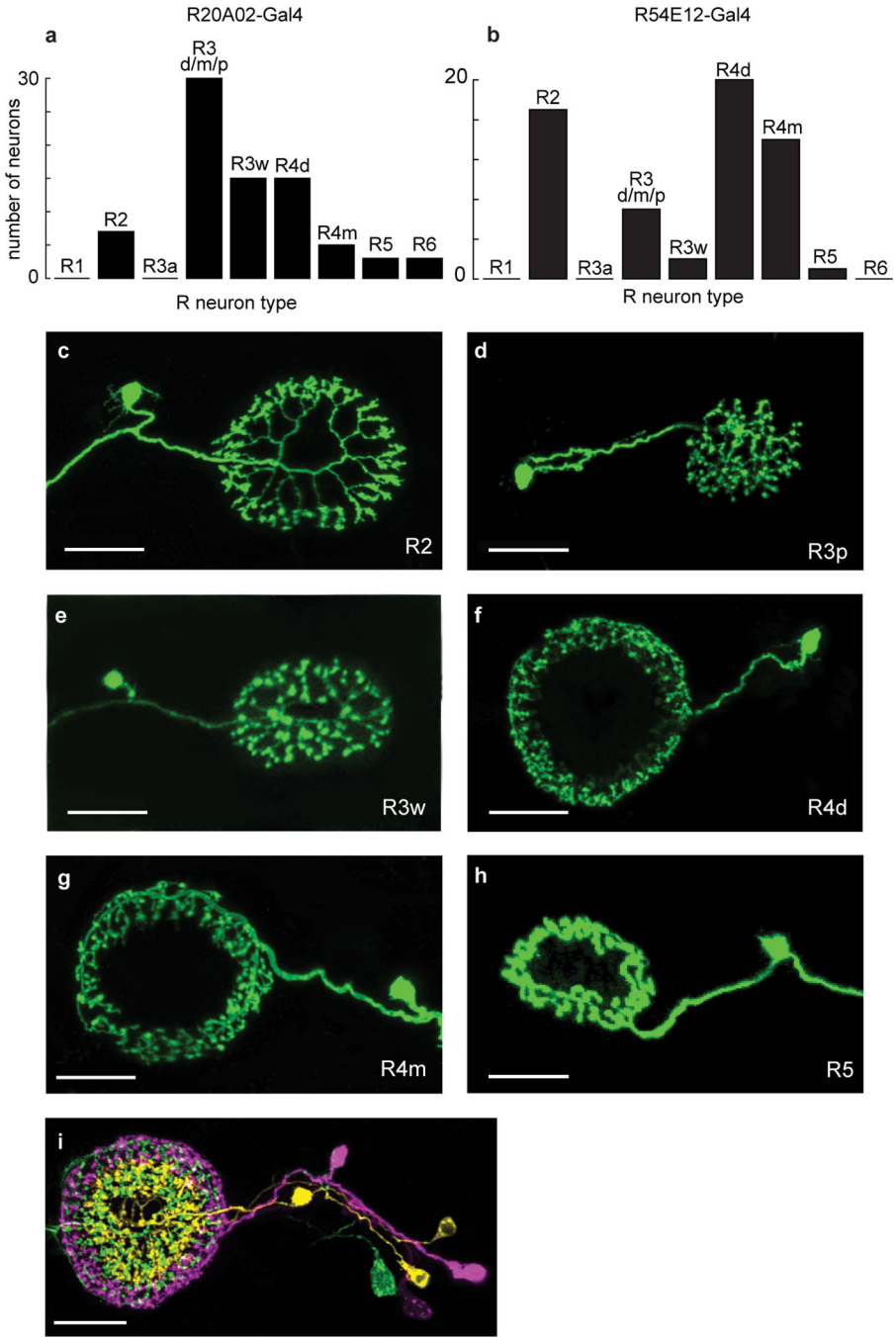

Extended Data Fig. 5: R neurons types labeled by *R20A02-Gal4* and *R54E12-Gal4* described by Multi-Color Flip-Out.

a. Observed numbers of R neurons belonging to each type from a dataset of n = 78 single-neuron Multi-Color Flp-Out clones[43] (MCFO) from the *R20A02-Gal4* line. R neuron types were classified according to Omoto et al.[6].

b. Same as (a) but for the *R54E12-Gal4* line (n = 61 single-neuron MCFO clones).

c-h. Examples of single R-neuron MCFO clones. Images are maximum intensity z-projections. Background labeling was manually removed to improve clarity of specific neuronal morphologies.

i. Multiple R-neuron MCFO clones labeled in different colors using the *R20A02-Gal4* line. Image is a maximum-intensity *z*-projection. Scale bars are 20 μm.

Extended Data Fig. 5 genotypes: *R57C10-FLPG5.PEST; UAS(FRT.stop)myr::smGdP-HA, UAS(FRT.stop)myr::smGdP-V5, UAS(FRT.stop)myr::smGdP-FLAG / R20A02-Gal4, R57C10-FLPG5.PEST; UAS(FRT.stop)myr::smGdP-HA, UAS(FRT.stop)myr::smGdP-V5, UAS(FRT.stop)myr::smGdP-FLAG / R54E12-Gal4*

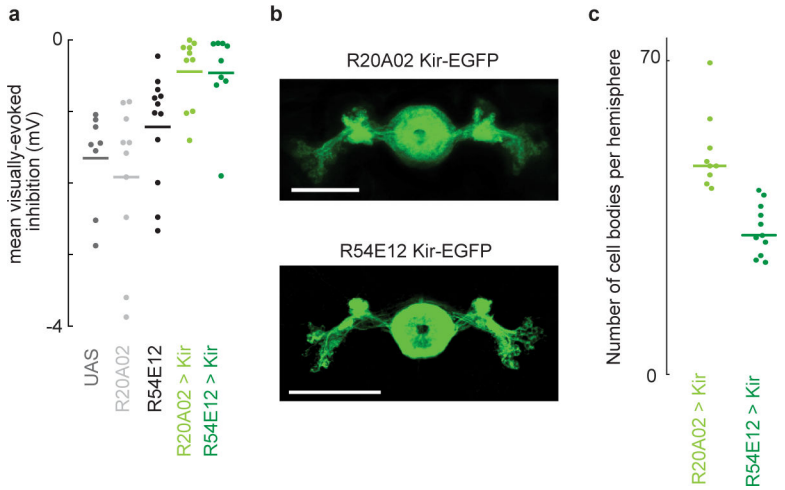

Extended Data Fig. 6: Suppressing R neuron activity with two independent driver lines reduces E-PG visually evoked hyperpolarization.

a. Same as Fig. 3c (right), except instead of measuring peak visually evoked hyperpolarization, we measured mean visually evoked hyperpolarization (by zeroing all non-negative visual responses and then averaging visual responses across all cue positions) n = 8, 10, 12, 10, 9). Both Kir means are significantly different from corresponding genetic controls using two-sided Wilcoxon rank-sum tests. *R20A02 Kir* vs. *R20A02* / + and *UAS* / + (p= 0.0013 and 0.0003), *R54E12 Kir* vs *R54E12* / + and *UAS* / + (p = 0.005 and 0.0025).

b. R neuron population labeled by Kir2.1::EGFP. Images are maximum intensity z-projections.

c. Numbers of R neurons per hemisphere expressing Kir2.1::EGFP in each experimental genotype n = 9 (*R20A02*), n = 11 (*R54E12*) (horizontal lines are means).

Based on the total number of R neurons of each type reported by Omoto et al.[6], and our MCFO quantification of the R neuron types labeled by *R20A02-Gal4* and *R54E12-Gal4* (Extended Data Fig. 5), these cell counts suggest that *R20A02-Gal4* targets approximately 20% of R2, 30% of R4m, and all R4d neurons. These counts suggest that *R20A02-Gal4* targets approximately 40% of R2 neurons and all R4m and R4d neurons. This incomplete targeting of outer R neurons may provide one explanation for the remaining visually evoked inhibition observed in some recordings (Fig. 3).

Note that while both driver lines label other neurons in the central brain and visual system, R neurons appear to be the only cell type that is labeled by both lines. In the visual system, driver line *R20A02-Gal4* targets one medulla intrinsic neuron, likely Mi12 and one cell type that arborizes in ~layer 4–6 of the lobula, while driver line *R54E12-Gal4* appears to target the medulla neuron Tm3.

Extended Data Fig. 6 genotypes: *+ / w; R60D05-LexA / LexAop-mCD8::GFP; + / UAS-Kir2.,* (UAS-only control), *+ / w; R60D05-LexA / LexAop-mCD8::GFP; R20A02-Gal4 /+* (R20A02 Gal4-only control), *+ / w; R60D05-LexA/LexAop-mCD8::GFP; R54E12-Gal4/+* (R54E12 Gal4-only control), *+ / w; R60D05-LexA / LexAop-mCD8::GFP; R20A02-Gal4/ UAS-Kir2.1* (R20A02 Kir), *+ / w; R60D05-LexA/LexAop-mCD8::GFP; R54E12-Gal4 / UAS-Kir2.1* (R54E12 Kir)

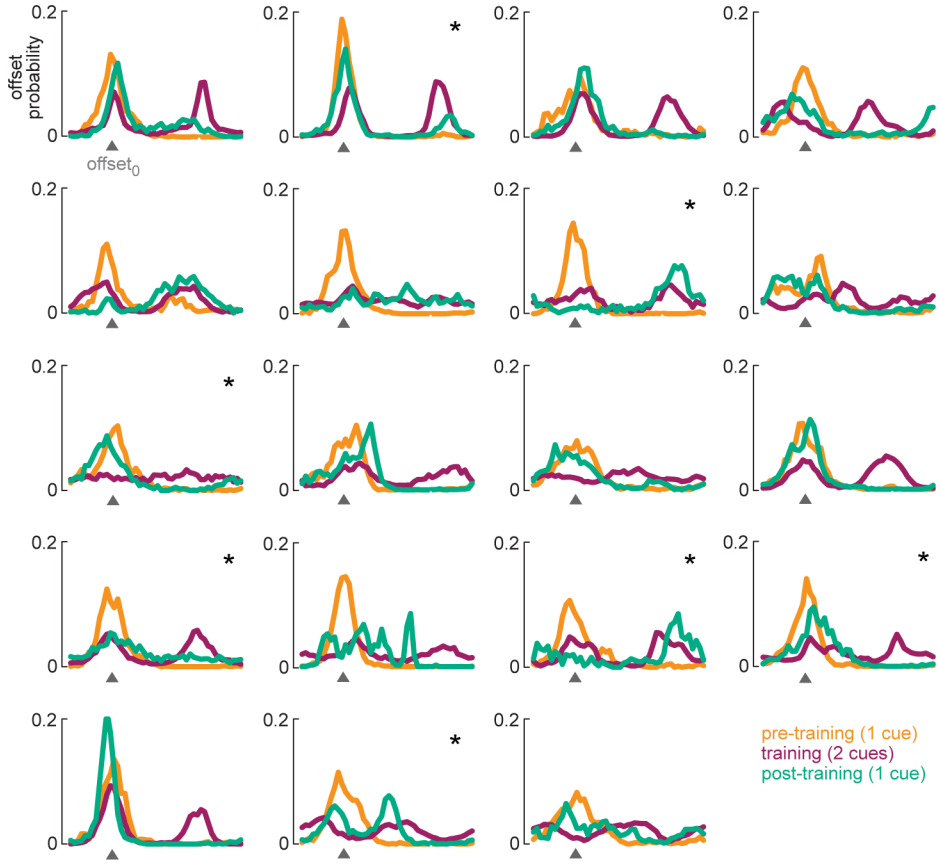

Extended Data Fig. 7: Offset probability histograms in training experiments.

Offset probability histograms during each segment of the training experiments shown in Fig. 4, for all 19 GCaMP imaging experiments (in 19 flies). As in Fig. 4, the circular mean during the pre-training period is defined as $offset_0$ (here marked with an arrowhead), and for display purposes we horizontally aligned all the $offset_0$ values in different flies. Asterisks mark data shown in Fig. 4.

Extended Data Fig. 7 genotype: + / *w; UAS-GCaMP6f / +; R60D05-Gal4 / +*

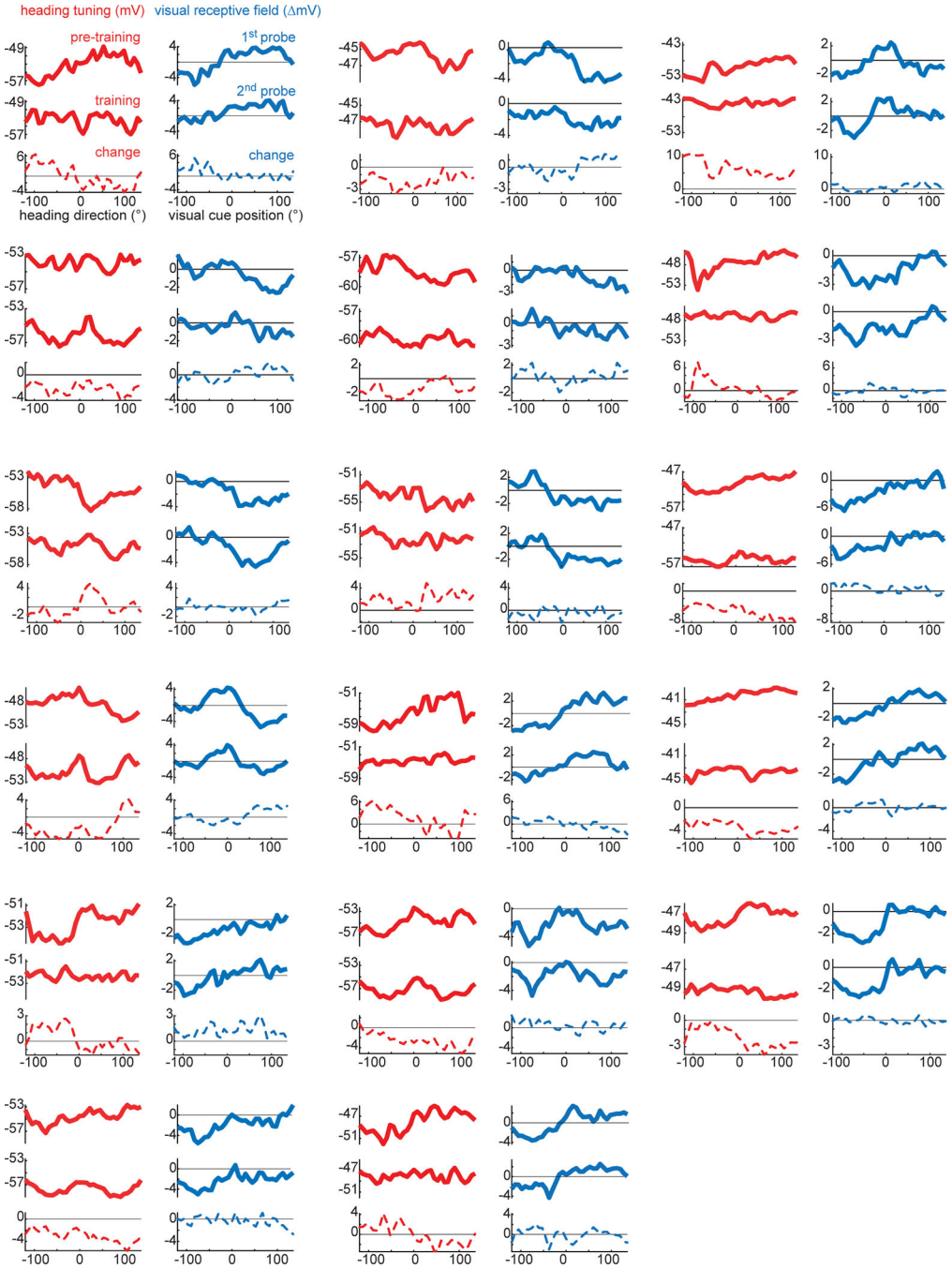

Extended Data Fig. 8: Heading tuning and visual receptive field measurements in training experiments.

Heading tuning curves and visual receptive fields for all additional 17 E-PG neurons (from 17 flies) from the training experiments in Fig. 5. As in Fig. 5, red solid curves are heading tuning. Red dashed curves are the change in heading tuning (training minus pre-training). Blue curves are visual receptive fields. Blue dashed curve is the change in the visual receptive field (2^{nd} probe minus 1^{st} probe). Seven neurons from this data set also appear in Figs. 1–2.

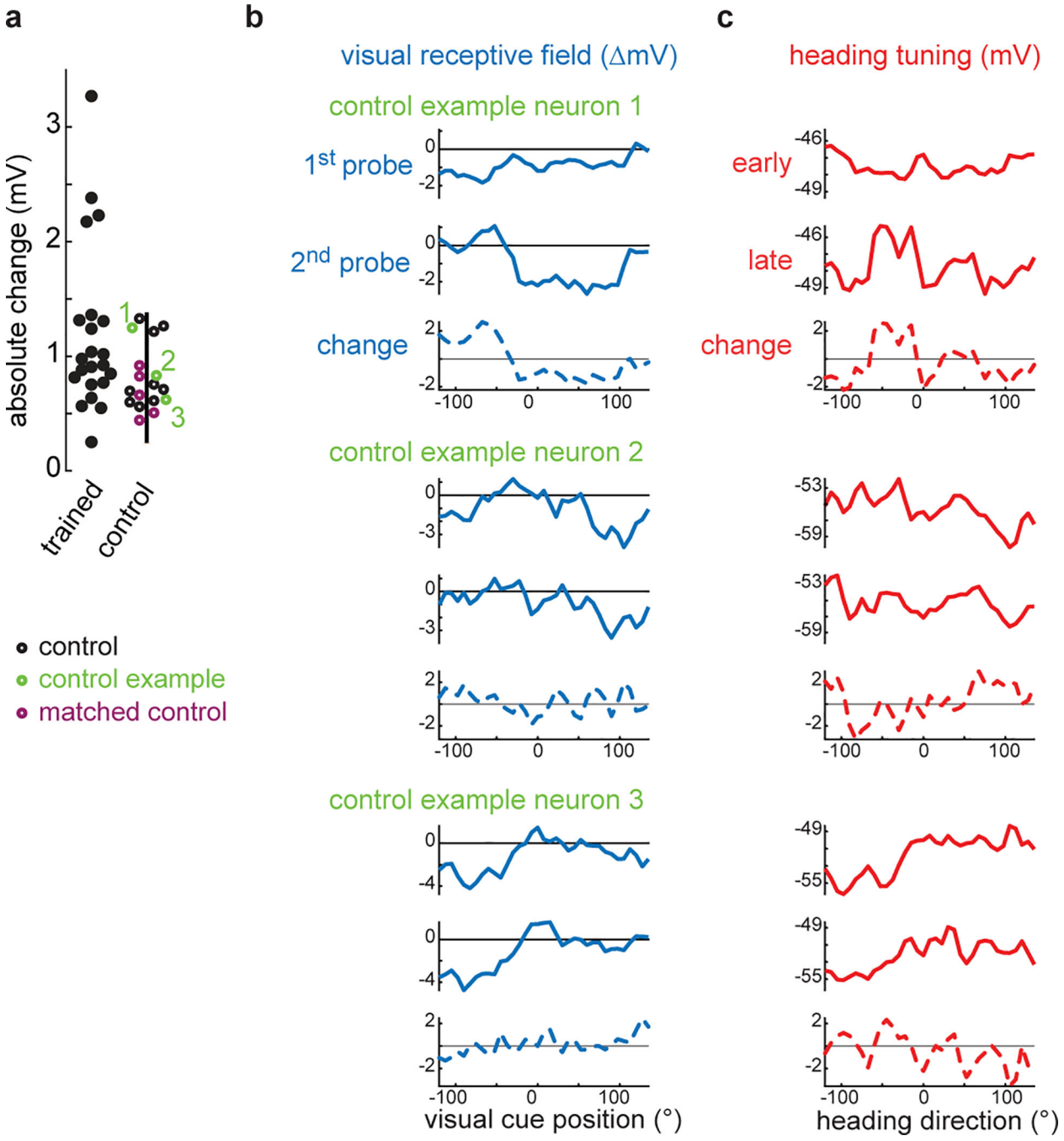

Extended Data Fig. 9: Controls for remapping experiments.

a. Data reproduced from Fig. 5e. Absolute change in visual receptive fields. Control flies navigated in a 1-cue world (rather than a 2-cue world) during the waiting period between the open-loop epochs used to compute the change in visual responses. In some cases ("matched control"), flies received exactly the same protocol as the experimental condition except with 1-cue closed-loop during the training period; in other words, these matched controls received 12 consecutive minutes of 1-cue (rather than 2-cue) closed-loop during the "training" period. In all other cases ("control"), flies received 4-minute blocks of 1-cue closed-loop interleaved

with 150-second open-loop epochs during the “training” period, which lasted 12 minutes or more.

b. Visual receptive fields from control cells. Blue dashed curve is the change in visual receptive field (2^{nd} probe – 1^{st} probe) over the control period. Typically, visual receptive fields were stable over time under control conditions (control neurons 2 and 3). On occasion, we observed spontaneous changes in an E-PG neuron’s visual receptive field during the control period (e.g., control neuron 1), although these changes were not as large as the changes we observed in many neurons in trained flies (see panel a).

c. Heading tuning in the same three control cells. Note how the spontaneous changes in visual receptive fields seen in neuron 1 are accompanied by changes in heading tuning.

Acknowledgements

We are grateful to David Anderson, Thomas Clandinin, Barret Pfeiffer, Gerald Rubin, and John Tuthill for providing fly stocks. Thomas Clandinin, Bruce Bean, Jan Drugowitsch, David Ginty, and Wilson lab members provided feedback on the manuscript and Jan Drugowitsch provided advice on data analysis. We are grateful to Gaby Maimon for sharing designs for a fly holder and modified FicTrac software. We thank Ofer Mazor and Pavel Gorelik at the Harvard Medical School Research Instrumentation Core (NEI Core Grant for Vision Research EY012196) for their help constructing the virtual reality systems. This work was supported by the Harvard Neurobiology Imaging Facility (NINDS P30 NS072030). This work was funded by NIH awards U19NS104655, F30DC017698 (J.L.), and T32GM007753 (J.L.). Y.E.F. is supported by a HHMI Hanna H. Gray Fellowship.. R.I.W. is an HHMI Investigator.

References

1. Seelig JD & Jayaraman V Neural dynamics for landmark orientation and angular path integration. Nature 521, 186–191, (2015) [PubMed: 25971509]
2. Kim SS, Rouault H, Druckmann S & Jayaraman V Ring attractor dynamics in the Drosophila central brain. Science 356, 849–853, (2017) [PubMed: 28473639]
3. Green J et al. A neural circuit architecture for angular integration in Drosophila. Nature 546, 101–106, (2017) [PubMed: 28538731]
4. Turner-Evans D et al. Angular velocity integration in a fly heading circuit. eLife 6, (2017)
5. Seelig JD & Jayaraman V Feature detection and orientation tuning in the Drosophila central complex. Nature 503, 262–266, (2013) [PubMed: 24107996]
6. Omoto JJ et al. Neuronal constituents and putative interactions within the Drosophila ellipsoid body neuropil. Front. Neural Circuits 12, 103, (2018) [PubMed: 30546298]
7. Skaggs WE, Knierim JJ, Kudrimoti HS & McNaughton BL A model of the neural basis of the rat’s sense of direction. Adv. Neural Inf. Process. Syst 7, 173–180, (1995) [PubMed: 11539168]
8. Milford MJ, Wyeth GF & Prasser D RatSLAM: A hippocampal model for simultaneous localization and mapping. In International Conference on Robotics and Automation, 403–408 (2004).
9. Mulas M, Waniek N & Conradt J Hebbian plasticity realigns grid cell activity with external sensory cues in continuous attractor models. Front. Comput. Neurosci. 10, 13, (2016) [PubMed: 26924979]
10. Cope AJ, Sabo C, Vasilaki E, Barron AB & Marshall JA A computational model of the integration of landmarks and motion in the insect central complex. PLoS One 12, e0172325, (2017) [PubMed: 28241061]
11. Keinath AT, Epstein RA & Balasubramanian V Environmental deformations dynamically shift the grid cell spatial metric. eLife 7, (2018)
12. Ocko SA, Hardcastle K, Giocomo LM & Ganguli S Emergent elasticity in the neural code for space. Proc. Natl. Acad. Sci. U. S. A, (2018)
13. Taube JS, Muller RU & Ranck JB Jr. Head-direction cells recorded from the postsubiculum in freely moving rats. I. Description and quantitative analysis. J. Neurosci 10, 420–435, (1990) [PubMed: 2303851]

14. Taube JS, Muller RU & Ranck JB Jr. Head-direction cells recorded from the postsubiculum in freely moving rats. II. Effects of environmental manipulations. J. Neurosci 10, 436–447, (1990) [PubMed: 2303852]
15. Mizumori SJ & Williams JD Directionally selective mnemonic properties of neurons in the lateral dorsal nucleus of the thalamus of rats. J. Neurosci 13, 4015–4028, (1993) [PubMed: 8366357]
16. Knierim JJ, Kudrimoti HS & McNaughton BL Place cells, head direction cells, and the learning of landmark stability. J. Neurosci 15, 1648–1659, (1995) [PubMed: 7891125]
17. Zhang K Representation of spatial orientation by the intrinsic dynamics of the head-direction cell ensemble: a theory. J. Neurosci 16, 2112–2126, (1996) [PubMed: 8604055]
18. Xie X, Hahnloser RH & Seung HS Double-ring network model of the head-direction system. Phys. Rev. E Stat. Nonlin. Soft Matter Phys 66, 041902, (2002) [PubMed: 12443230]
19. Hanesch U, Fischbach KF & Heisenberg M Neuronal architecture of the central complex nin Drosophila melanogaster. Cell Tissue Res 257, 343–366, (1989)
20. Zhang Z, Li X, Guo J, Li Y & Guo A Two clusters of GABAergic ellipsoid body neurons modulate olfactory labile memory in Drosophila. J. Neurosci 33, 5175–5181, (2013) [PubMed: 23516283]
21. Jacob PY et al. An independent, landmark-dominated head-direction signal in dysgranular retrosplenial cortex. Nat. Neurosci 20, 173–175, (2017) [PubMed: 27991898]
22. Kim SS, Hermundstad AM, Romani S, Abbott LF & Jayaraman V The flexible generation of a stable heading representation in diverse visual scenes. Nature in press, (2019)
23. Cadena C et al. Past, present, and future of simultaneous localization and mapping: toward the robust-perception age. IEEE Transactions on Robotics 32, 1309–1332, (2016)
24. Sun Y et al. Neural signatures of dynamic stimulus selection in Drosophila. Nat. Neurosci 20, 1104–1113, (2017) [PubMed: 28604683]
25. Wehner R Astronavigation in insects. Annu. Rev. Entomol 29, 277–298, (1984)
26. Wehner R & Muller M The significance of direct sunlight and polarized skylight in the ant's celestial system of navigation. Proc Natl Acad Sci U S A 103, 12575–12579, (2006) [PubMed: 16888039]
27. el Jundi B, Smolka J, Baird E, Byrne MJ & Dacke M Diurnal dung beetles use the intensity gradient and the polarization pattern of the sky for orientation. J. Exp. Biol 217, 2422–2429, (2014) [PubMed: 24737763]
28. el Jundi B, Foster JJ, Byrne MJ, Baird E & Dacke M Spectral information as an orientation cue in dung beetles. Biol. Lett 11, (2015)
29. Bell WJ, Tobin TR & Sorensen KA Orientation responses of individual larder beetles, *Dermestes ater* (Coleoptera, Dermestidae), to Directional shifts in wind stimuli. J. Insect Behav 2, 787–801, (1989)
30. Heinzel H-G & Böhm H The wind-orientation of walking carrion beetles. J. Comp. Physiol. [A]. 1989, 775–786, (1989)
31. el Jundi B et al. Neural coding underlying the cue preference for celestial orientation. Proc. Natl. Acad. Sci. U. S. A 112, 11395–11400, (2015) [PubMed: 26305929]
32. Pegel U, Pfeiffer K & Homberg U Integration of celestial compass cues in the central complex of the locust brain. Curr. Biol 221, jeb171207, (2018)
33. Muller M & Wehner R Wind and sky as compass cues in desert ant navigation. Naturwissenschaften 94, 589–594, (2007) [PubMed: 17361400]
34. el Jundi B et al. A snapshot-based mechanism for celestial orientation. Curr. Biol 26, 1456–1462, (2016) [PubMed: 27185557]
35. Dacke M et al. Multimodal cue integration in the dung beetle compass. Proc Natl Acad Sci U S A 116, 14248–14253, (2019) [PubMed: 31235569]
36. Jammalamadaka SR & SenGupta A Topics in circular statistics. (World Scientific, 2001).

References for Online Methods

37. Jenett A et al. A GAL4-driver line resource for Drosophila neurobiology. Cell Rep 2, 991–1001, (2012) [PubMed: 23063364]

38. Wang J, Zugates CT, Liang IH, Lee CH & Lee T Drosophila Dscam is required for divergent segregation of sister branches and suppresses ectopic bifurcation of axons. Neuron 33, 559–571, (2002) [PubMed: 11856530]
39. Pfeiffer B et al. Refinement of tools for targeted gene expression in Drosophila. Genetics 186, 735–755, (2010) [PubMed: 20697123]
40. Hoopfer ED, Jung Y, Inagaki HK, Rubin GM & Anderson DJ P1 interneurons promote a persistent internal state that enhances inter-male aggression in Drosophila. eLife 4, (2015)
41. Hardie RC et al. Calcium influx via TRP channels is required to maintain PIP2 levels in Drosophila photoreceptors. Neuron 30, 149–159, (2001) [PubMed: 11343651]
42. Chen TW et al. Ultrasensitive fluorescent proteins for imaging neuronal activity. Nature 499, 295–300, (2013) [PubMed: 23868258]
43. Nern A, Pfeiffer BD & Rubin GM Optimized tools for multicolor stochastic labeling reveal diverse stereotyped cell arrangements in the fly visual system. Proc. Natl. Acad. Sci. U. S. A 112, E2967–2976, (2015) [PubMed: 25964354]
44. Goodman MB & Lockery SR Pressure polishing: a method for re-shaping patch pipettes during fire polishing. J. Neurosci. Methods 100, 13–15, (2000) [PubMed: 11040361]
45. Green J, Vijayan V, Mussells Pires P, Adachi A & Maimon G Walking Drosophila aim to maintain a neural heading estimate at an internal goal angle. bioRxiv, doi: 10.1101/315796, (2018)
46. Gouwens NW & Wilson RI Signal propagation in Drosophila central neurons. J. Neurosci 29, 6239–6249, (2009) [PubMed: 19439602]
47. Wolff T, Iyer NA & Rubin GM Neuroarchitecture and neuroanatomy of the Drosophila central complex: A GAL4-based dissection of protocerebral bridge neurons and circuits. J. Comp. Neurol 523, 997–1037, (2015) [PubMed: 25380328]
48. Moore RJ et al. FicTrac: a visual method for tracking spherical motion and generating fictive animal paths. J. Neurosci. Methods 225, 106–119, (2014) [PubMed: 24491637]
49. Reiser MB & Dickinson MH A modular display system for insect behavioral neuroscience. J. Neurosci. Methods 167, 127–139, (2008) [PubMed: 17854905]
50. Klapoetke NC et al. Independent optical excitation of distinct neural populations. Nat Methods 11, 338–346, (2014) [PubMed: 24509633]
51. Schindelin J et al. Fiji: an open-source platform for biological-image analysis. Nat Methods 9, 676–682, (2012) [PubMed: 22743772]
52. Buchanan SM, Kain JS & de Bivort BL Neuronal control of locomotor handedness in Drosophila. Proc. Natl. Acad. Sci. U. S. A 112, 6700–6705, (2015) [PubMed: 25953337]
53. Pnevmatikakis EA & Giovannucci A NoRMCorre: An online algorithm for piecewise rigid motion correction of calcium imaging data. J. Neurosci. Methods 291, 83–94, (2017) [PubMed: 28782629]

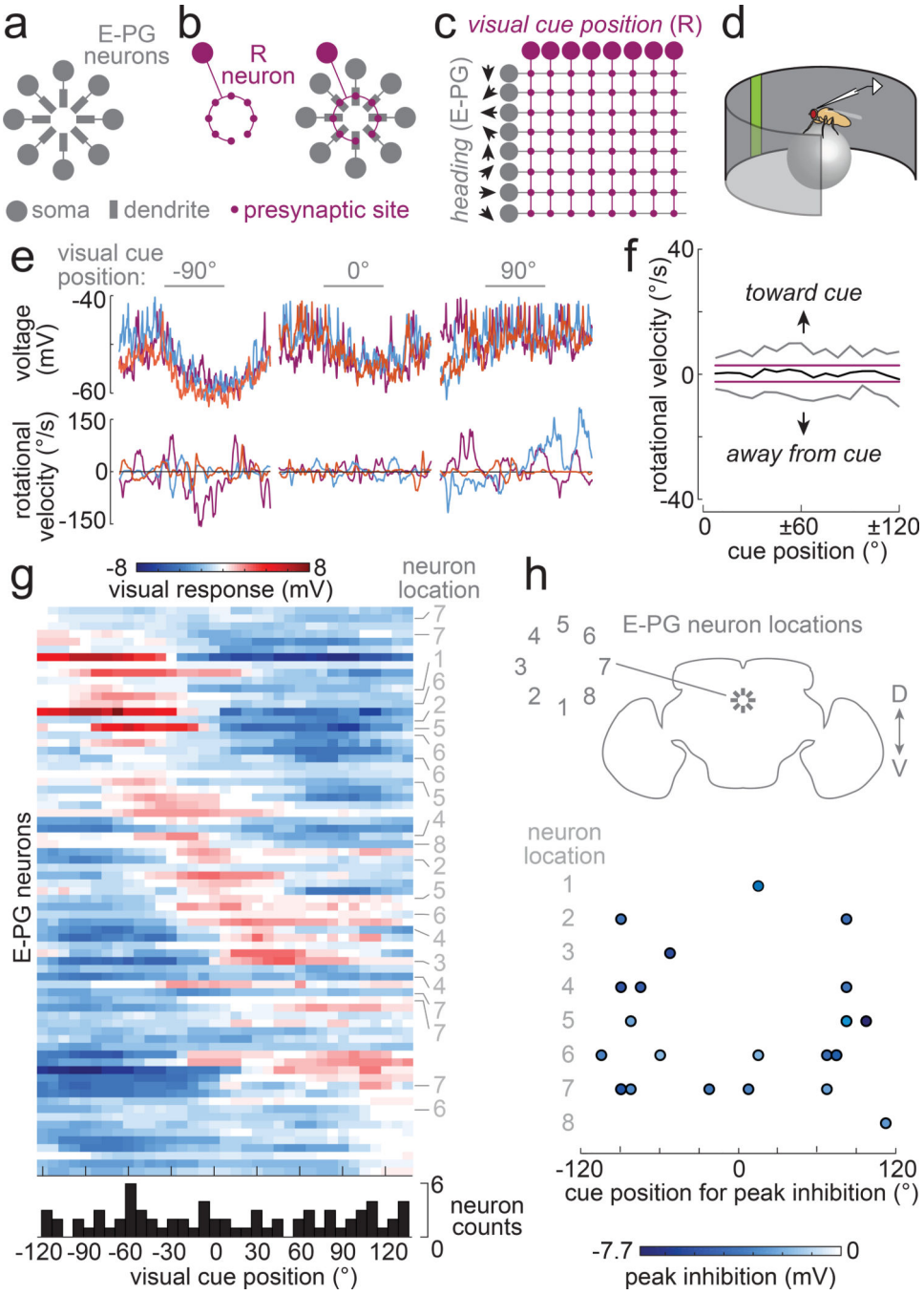

Figure 1: E-PG neurons are inhibited by visual cues at specific positions.

a. Schematic: E-PG neuron dendrites form a circular array, with adjacent cells representing adjacent headings.

b. Schematic: each R neuron axon forms a ring (left) which overlaps all E-PG dendrites (right).

c. Schematic: an unwrapped R→E-PG matrix.

d. Schematic: an E-PG neuron is recorded in whole-cell mode while the fly walks on a ball, surrounded by a panorama where a cue flashes at random horizontal positions.

e. Top: three example E-PG responses per cue position, for three different positions, all from the same recording. Bottom: fly's yaw velocity (+ right, − left). Note that the fly behaves differently on different trials, but the neural response is essentially the same regardless of the fly's behavior. Cue flash is 500 ms.

f. Fly's rotational velocity around cue presentation, mean (black) ± 1 standard deviation (gray) across flies. Magenta lines show bootstrapped 95% confidence interval of the mean across flies after randomizing cue positions, Bonferroni-corrected; because the mean lies within these bounds, it is not significantly different from random.

g. Summary of E-PG visual receptive fields (73 neurons in 68 flies). Cells are sorted by the cue position that evoked the most positive (least negative) response. Histogram counts cells preferring each cue position. Some cells were filled to determine their location (see h).

h. Cue position eliciting peak inhibition, versus neuron location (no significant correlation: circular correlation coefficient = 0.097, p = 0.66, n=21; see Extended Data Fig. 2g and ref. [36]).

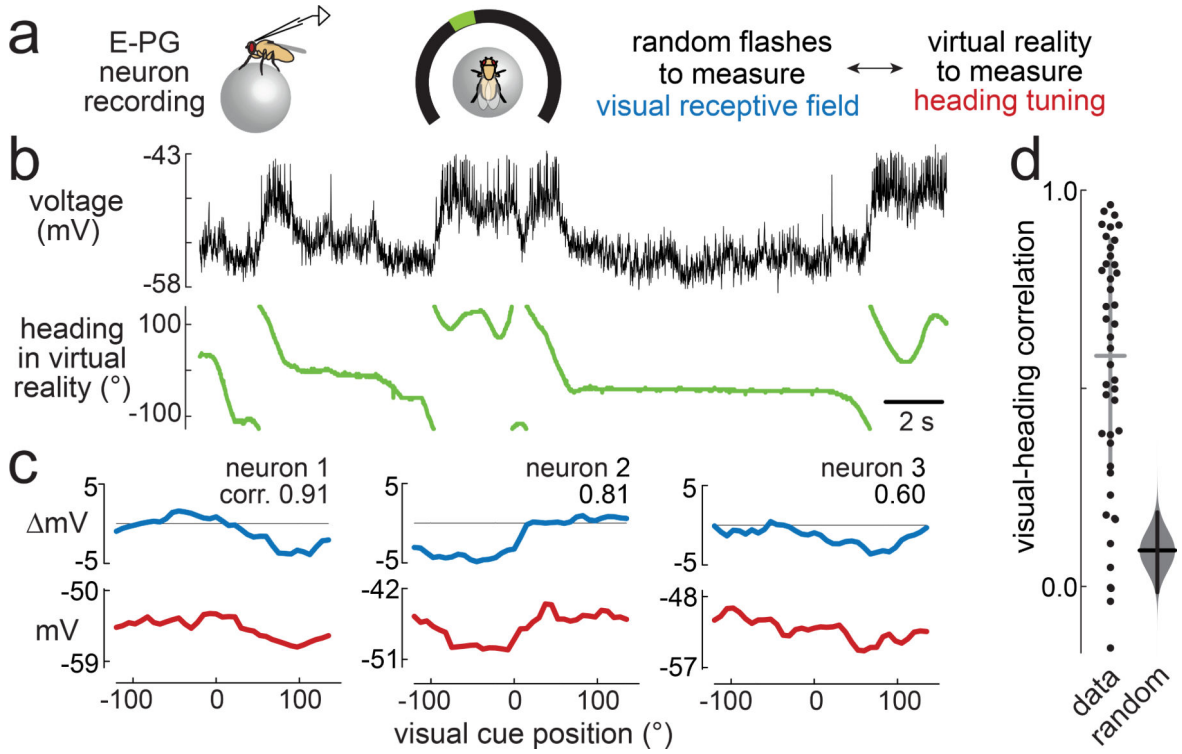

Figure 2: E-PG neuron visual receptive fields align with heading tuning.

a. Schematic: interleaved blocks measuring the visual receptive fields and heading tuning.

b. Top: E-PG voltage during a virtual reality (VR) epoch. Bottom: VR heading. A heading of 0° means the cue is in front of the fly.

c. Comparison of visual receptive field and heading tuning from three example E-PG neurons (from 3 flies, with Pearson's correlation coefficients).

d. Pearson's correlation coefficients from 40 cells in 39 flies (all cells from Fig. 1). The mean and 95% confidence internal (CI) are shown as horizontal/vertical lines. The mean of the data is outside the 95% CI of a bootstrap distribution (gray violin plot) computed on randomized visual-heading pairings.

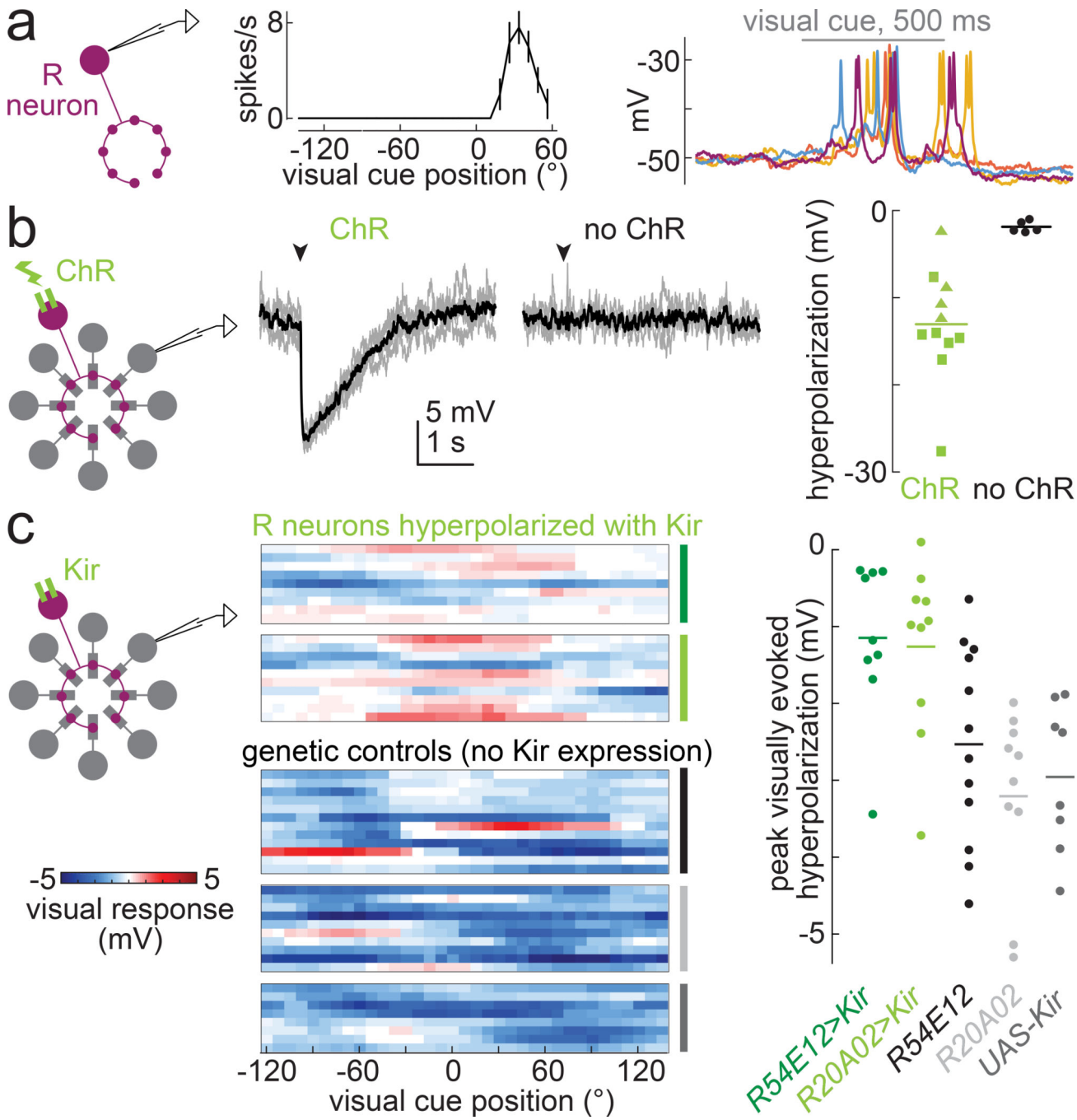

Figure 3: R neurons drive visually evoked inhibition in E-PG neurons.

a. Left: visually evoked spike rates in an R neuron (mean ± SEM across trials, n = 5–6 trials, R2 neuron). Right: four responses to repeated presentation of the best cue position for this neuron. We observed spatially tuned responses in 3 of 7 R2 cells and 1 of 3 R4d cells; an additional 3 R2 cells and 1 R4d cell responded to full field illumination but were unresponsive to the cue or not spatially tuned.

b. Left: responses of an E-PG neuron to optogenetic activation of R2 neurons via Chrimson (ChR), with four single trials in gray, mean in black. Middle: same but with no ChR in R

neurons, n= 4 trials. Right: summary of mean evoked hyperpolarization with ChR in R neurons (■ R2 neurons, n=7; ▲ R4d neurons, n=4) and controls (n=5).

c. Left: E-PG visual receptive fields in flies where R neurons were hyperpolarized using Kir2.1 expression driven by *R54E12-Gal4* or *R20A02-Gal4* (green shades) versus controls (*R54E12-Gal4*-only, *R20A02-Gal4*-only, *UAS-Kir*-only, gray shades). Right: summary of peak visually evoked hyperpolarization, color coded as before (horizontal lines are means; n = 8, 10, 12, 10, 9 cells; *R54E12 Kir* versus *R54E12 / +* and *UAS* / +, p = 0.021 and 0.0016; *R20A02 Kir* versus *R20A02* / + and *UAS* / +, p= 0.0046 and 0.012; two-sided Wilcoxon rank-sum tests).

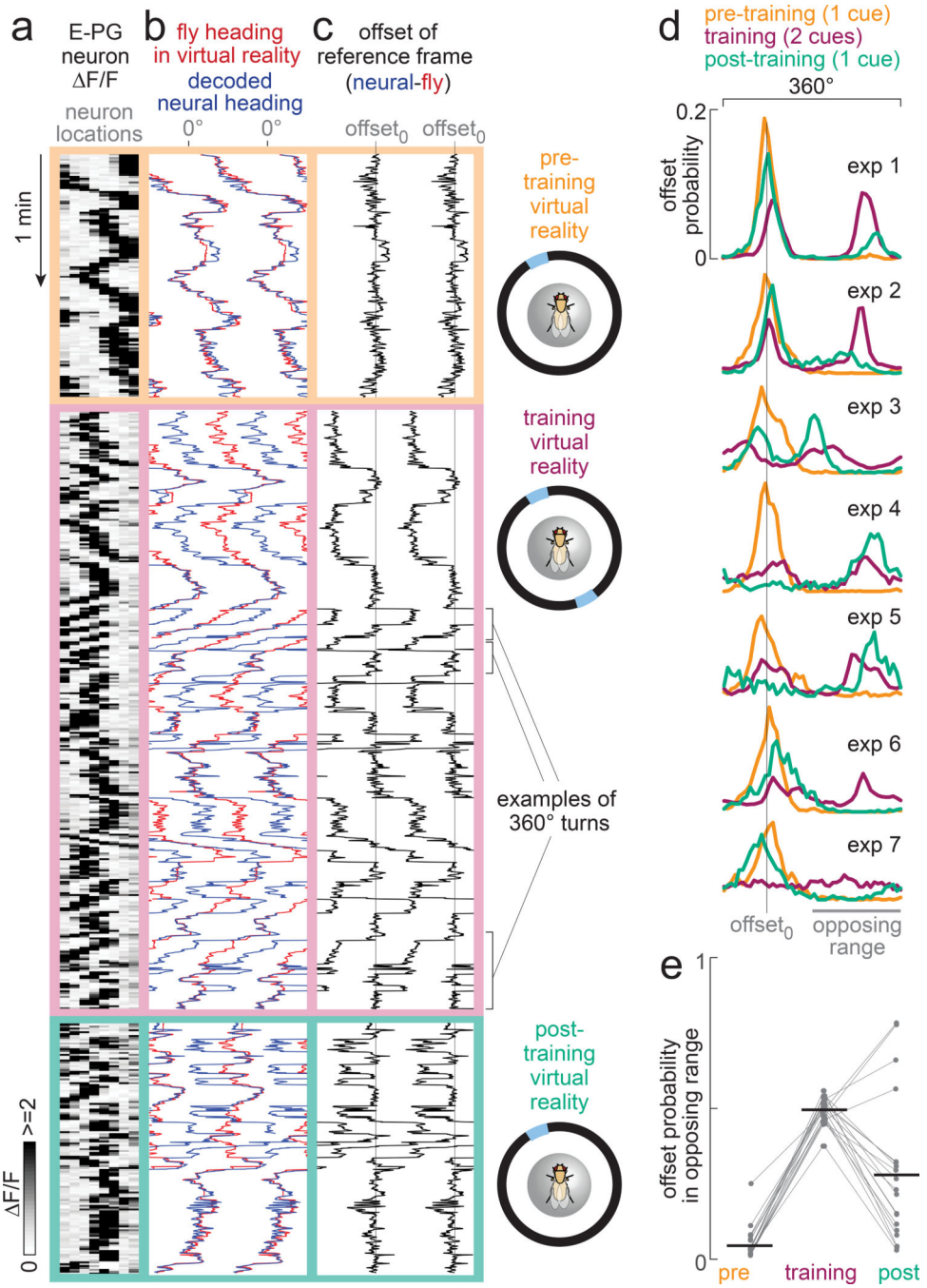

Figure 4: Visuomotor experience can persistently change ensemble heading direction representations.

a. E-PG ensemble GCaMP6f signals. Here the circular E-PG ensemble has been linearized, with each row showing 8 sectors of the ensemble. The fly walked in a 1-cue environment (pre-training, ≥10 min), then a 2-cue environment (training, 20 min), and finally a 1-cue environment (post-training, ≥4 min). Three snippets of one experiment are shown. Brackets mark 360° turns when the bump skipped over half the ensemble.

b. In the same experiment, VR heading (red) overlaid with the decoded neural representation of heading (blue). We double-plotted both traces and shifted the entire red trace horizontally so it overlapped with the blue trace during pre-training.

c. The offset of the neural representation of heading relative to the fly heading, double-plotted. The circular mean during pre-training is marked with a vertical line (defined as $offset_0$).

d. Offset probability histograms during each block, for seven example experiments. We found diverse values of $offset_0$ in different flies, as reported previously[1], but for display we horizontally aligned all $offset_0$ values in different flies. The "opposing range" is the range from ($offset_0$ + 90°) to ($offset_0$ − 90°). Examples 1–5 show a phase change post-training.

e. Total offset probability in the opposing range. Each set of connected points is one experiment (n=19 flies). Training and post-training are both significantly different from pre-training ($p=3.8\times10^{-6}$ training vs pre-training and $p=5.31^{-5}$ post-training vs pre-training, two-sided exact paired Wilcoxon signed rank tests).

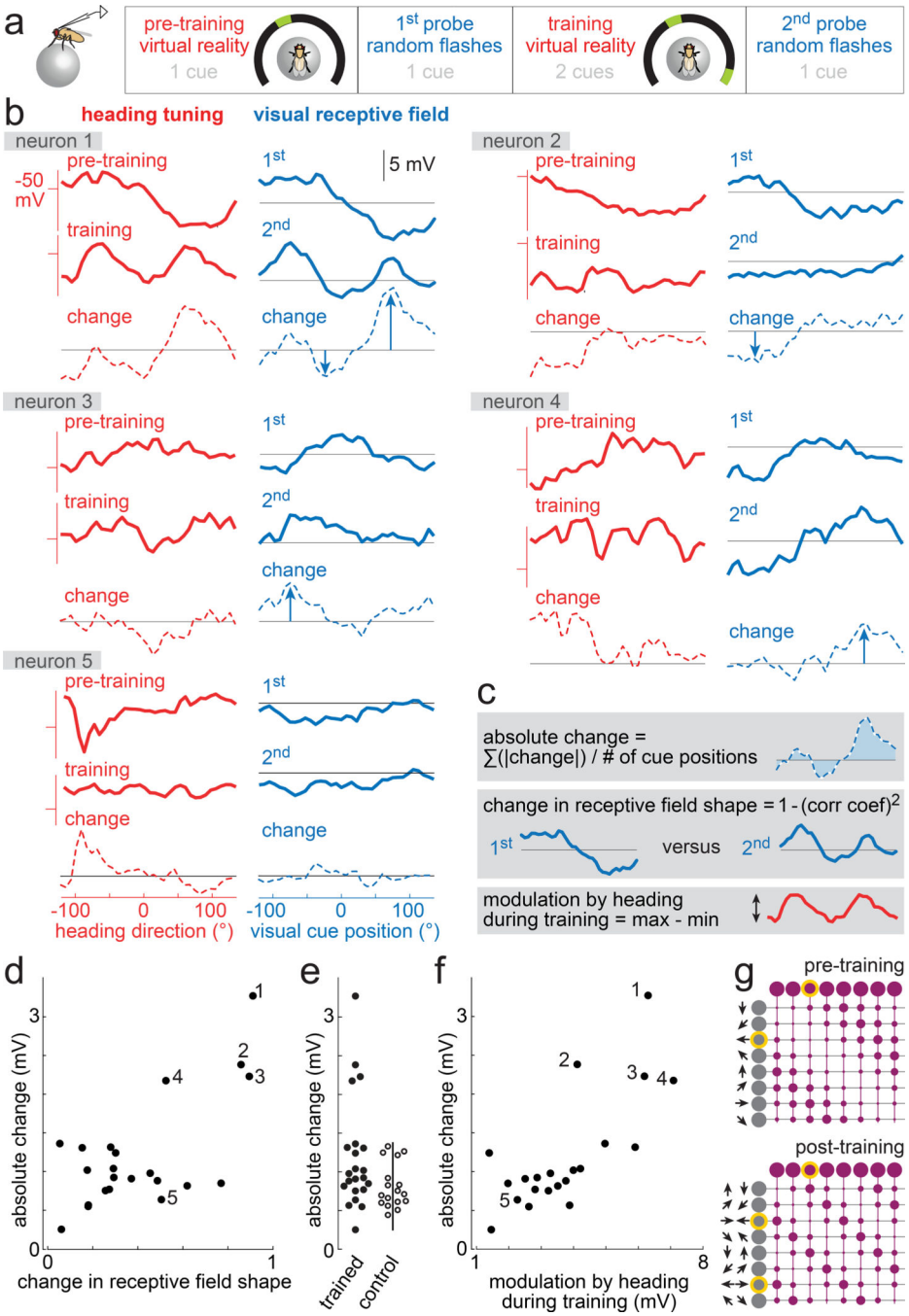

Figure 5: Visuomotor experience can remap visual input to E-PG neurons contingent on postsynaptic activity.

a. After the fly navigated in VR with one cue (pre-training), we measured the E-PG visual receptive field (1st probe). Then the fly navigated in VR with two cues for 12 min (training) and we again measured the visual receptive field (2nd probe).

b. Five example neurons. Red solid curves are heading tuning (red tick is −50 mV). Red dashed curve is the change in heading tuning (training minus pre-training). Blue solid curves are visual receptive fields. Blue dashed curve is the change in visual receptive fields (2nd

probe minus 1st probe). Arrowheads mark large changes. Neuron 5 is an example with little modulation by heading during training and little change in visual receptive field.

c. Explanation of metrics in (d-f).

d. Absolute change in visual receptive fields, versus change in receptive field shape (R^2 = 0.44, p = 0.00078 testing t-statistic slope ≠ 0, 22 E-PG neurons in 22 flies).

e. Absolute change in visual receptive fields post-training (22 E-PG neurons in 22 flies) versus controls (17 E-PG neurons in 17 flies). Training is significantly different from control (p= 0.043, two-sided Wilcoxon rank-sum test). Controls walked in a one-cue VR (not two-cue VR) between the 1st and 2nd probe. Four training experiments had changes significantly larger than any controls (>2 SDs above control mean, vertical bar); these are neurons 1–4.

f. Absolute change in visual receptive fields, versus modulation by heading during training (R^2 = 0.52, p = 0.00016 testing t-statistic slope ≠ 0, 22 E-PG neurons in 22 flies).

g. Schematic of model. When a visual cue appears, it activates specific R neurons (highlighted magenta cell), and this pushes the bump toward the E-PG neuron with minimal inhibition (highlighted gray cell). Training changes R→E-PG weights so the bump toggles between two offsets during post-training. R neurons are ordered by receptive field position.